UCL Université catholique de Louvain

École polytechnique de Louvain (EPL)

3D characterization of the composition and mechanical properties of the bone-tendon interface

Dissertation presented by
Lisa LEYSSENS

for obtaining the Master's degree in
Biomedical Engineering

Supervisor(s)
Greet KERCKHOFS

Reader(s)
Thomas PARDOEN, Renaud RONSSE

Academic year 2017-2018

Acknowledgments

First, I would like to thank my supervisor, Pr. Greet Kerckhofs. She truly helped me in the research and dissertation of this thesis, putting a lot of time and effort in guiding me. Her follow-up all along the year and knowledge in the field have allowed me to complete this thesis.

I also would like to thank Sophie Ryelandt, who was present on a daily basis to help me with my experiments in the lab. She first helped me find a methodology to prepare my samples, for which a lot of brainstorming and creativity was required, and then she taught me everything about the nanoindenter.

I want to thank Pascale Lipnik, who, with all her knowledge in the field of biology and her enthusiasm, devoted a large amount of her time during my last month of research to help me prepare my samples.

Finally, I want to thank Carla Geeroms, who taught me how to dissect my samples and helped me with the micro-computed tomography experiments in Leuven, Audrey Favache who gave me a lot of advise on nanoindentation, and Charlotte Moens, who taught me how to use a cryostat. I am very grateful for all their help.

Abstract

Connective tissue injuries occurring at the interface between soft tissue and bone, also called the bone-tendon interface, commonly result in pain, disability and significant medical costs [1]. These injuries are commonly caused by sports activities or can be seen in elderly people, making them less mobile because of the inability to move without pain. The chances of failure of surgical reattachment are very high which makes the bone-tendon interface an important research topic [2]. To address this clinical issue, it is necessary to regenerate a tissue that has the same properties as the original one. Before this is possible, it is important to understand the properties of the tissue that needs to be replaced. That is why the purpose of this thesis is to characterize the composition and mechanical properties of the Achilles tendon-to-bone interface.

X-ray microfocus computed tomography and contrast-enhanced micro-computed tomography are used to determine the three-dimensional structure and composition of the interface while nanoindentation is used to study the mechanical properties. Age-related changes at the interface are investigated, as well as the influence of obesity-driven type 2 diabetes. The three aforementioned investigation methods are therefore applied to three different groups of mice: young mice, aged mice, and aged mice with diet-induced obesity.

Results from X-ray microfocus computed tomography show differences in the dimensions of the interface, especially the diabetic group is different. Contrast-enhanced computed tomography allows to observe collagen fiber orientation at the interface. Nanoindentation has only quite recently emerged as a technique for analyzing biological samples and is still in an early stage of development [3], requiring optimization of a protocol for sample preparation, which is not necessarily the same for all groups. Finally, testing parameters for indenting biological tissue also need to be optimized.

Contents

Acknowledgments i

Abstract ii

List of figures v

List of tables viii

List of abbreviations ix

1 Introduction 1

2 State of the art 2
2.1 Structure and composition of the interface . . . 2
2.2 Effect of ageing on bone-tendon interface . . . 4
2.3 Effect of type 2 diabetes on bone-tendon interface . . . 4
2.4 Available methods for characterization . . . 5

3 Problem statement and objectives 8
3.1 Problem statement . . . 8
3.2 Objectives of the thesis . . . 8

4 X-ray microfocus computed tomography 10
4.1 Principle of μCT . . . 10
4.1.1 Components . . . 10
4.1.2 Acquisition . . . 11
4.1.3 CE-CT . . . 11
4.2 Materials and methods . . . 11
4.2.1 Animal samples . . . 11
4.2.2 Sample preparation . . . 12
4.2.3 μCT image acquisition . . . 12
4.2.4 μCT and CE-CT image analysis . . . 13
4.2.5 Statistical analysis . . . 14
4.3 Results and discussion . . . 15
4.3.1 μCT . . . 16
4.3.2 CE-CT . . . 21
4.4 Conclusion . . . 24

5 Nanoindentation 25
5.1 Principle of nanoindentation . . . 25
5.2 Materials and methods . . . 26
5.2.1 Nanoindenter . . . 26

5.2.2 Sample preparation 28
5.2.3 Testing parameters 30
5.3 Results and discussion 31
5.3.1 Optimization of the sample preparation 31
5.3.2 Mechanical properties of bone-tendon interface 34
5.4 Conclusion 45

6 Conclusion **46**
6.1 General discussion 46
6.2 Future perspectives 47
6.2.1 μCT and CE-CT 47
6.2.2 Nanoindentation 48
6.3 Final conclusion 48

Bibliography **50**

Appendix A **53**

List of Figures

2.1 The anatomy of the bone-tendon interface [4]. 3
2.2 Model of the natural bone-tendon interface (left) and bone-tendon interface after healing (right) for the human supraspinatus insertion [5]. 4

4.1 General set-up of a μCT system 10
4.2 Light microscopy of a typical dissected and cleaned muring Achilles bone-tendon sample. The white part in the lower right part of the figure is the Achilles tendon (indicated by T), the darker part in the upper part of the image is the heel bone (indicated by B). I indicates the interface 11
4.3 The Phoenix Nanotom® m 12
4.4 Screenshot of CTAn software showing an ROI, indicated in blue, drawn on a transverse image of a dataset obtained from a young mouse sample 13
4.5 Screenshot of CTAn software showing how the contact length was measured for one ROI image obtained from a young mouse sample, the red line is the contact length 14
4.6 Coronal, sagittal and transverse views from μCT scans before and after staining (CE-CT) for a young mouse sample. B is bone, T is tendon and MF is mineralized fibrocartilage. 15
4.7 Left: Close-up view of the interface of a young sample. Right: same image showing the clear separation between regions 16
4.8 Left: Close-up view of the interface of an AM sample. Right: same image showing the clear separation between regions 17
4.9 Left: Close-up view of the interface of a DIO sample. Right: same image showing the clear separation between regions 17
4.10 The MF (VOI) computed with the CTAn software and represented in 3D with the CTVox software 17
4.11 Graphs comparing differences in volume and in number of pores of the MF in the three groups 18
4.12 Graph comparing the pore density in the MF for all groups 19
4.13 Graph comparing the mean and maximum thickness of the MF for all groups . . 19
4.14 Graph comparing the length of the interface between MF and NMF for all groups 20
4.15 Graph comparing the thickness of the tendon for all groups 21
4.16 Coronal and sagittal views of fiber orientation for Young sample with a zoom on the bone-tendon interface. T = tendon, B = bone 22
4.17 Coronal and sagittal views of fiber orientation for AM sample with a zoom on the bone-tendon interface. T = tendon, B = bone 22
4.18 Coronal and sagittal views of fiber orientation for DIO sample with a zoom on the bone-tendon interface and on the tendon. T = tendon, B = bone 23
4.19 Comparison before and after staining of a DIO sample, highlighting fiber orientation in the MF 24

5.1 Typical load-displacement curve and indentation process [3] 26

5.2 The *Agilent Nano Indenter G200*. A = sample tray, B = microscope, C = indentation tip, D = moving platform 27
5.3 Scheme of sample preparation for nanoindentation (step 1) - Method B 29
5.4 Scheme of sample preparation for nanoindentation (step 2) - Method B 29
5.5 Scheme of sample preparation and nanoindentation, as seen from the top - Method D 30
5.6 SEM image of embedded and polished sample - Method A 31
5.7 SEM image of embedded and polished sample - Method B. T = tendon and B = bone 32
5.8 Results of sample preparation - Method C. T = tendon and B = bone 32
5.9 Polarized light microscopy of microtome slice of bone-tendon interface - Method D. B = bone, T = tendon 33
5.10 DIC microscopy images of tendon and bone - Method D 33
5.11 Sample holder 34
5.12 Set-up of the sample ready for indentation 34
5.13 Modulus of resin in function of displacement 35
5.14 Typical load displacement curve for bone and for tendon 35
5.15 Modulus as a function of depth in the bone for a series of indents in a young sample. The green line is the modulus of resin. Method: Displacement control . 36
5.16 Value of the mean modulus between 700 and 1000 nm for indents in the bone of a young sample. Color scale unit is GPa. Black = indent not detected. B = bone . 36
5.17 Modulus as a function of depth in the tendon for a young sample. Green line is resin. Method: Displacement control 37
5.18 Value of the mean modulus between 700 and 1000 nm for indents in the tendon of a young sample. Color scale unit is GPa. Black = indent not detected. T = tendon 37
5.19 Load displacement curves for indents performed at the interface. Method: Displacement control 38
5.20 Modulus as a function of depth at the interface for a young sample. Blue lines are tendon, red lines bone, and light blue is interface. Method: Displacement control 38
5.21 Value of the mean modulus between 700 and 1000 nm for indents at the interface, in a young sample. Color scale unit is GPa. Black = indent not detected. T = tendon and B = bone 39
5.22 Modulus as a function of depth in the bone for an AM sample. Green line is resin. Method: Displacement control with increased DSC 39
5.23 Value of the mean modulus between 700 and 1000 nm for indents in the bone of an AM sample. Color scale unit is GPa. B = bone 40
5.24 Modulus as a function of depth in the bone for a DIO sample. Green line is resin. Method: Displacement control with increased DSC 40
5.25 Value of the mean modulus between 700 and 1000 nm for indents in the bone, in a DIO sample. Color scale unit is GPa. Black = indent not detected. B = bone . 40
5.26 Modulus as a function of depth in the tendon for an AM sample. Green line is resin. Method: Displacement control with increased DSC 41
5.27 Value of the mean modulus between 700 and 1000 nm for indents in the tendon, in an AM sample. Color scale unit is GPa. T = tendon 41
5.28 Image of the tendon in a DIO sample taken with the nanoindenter microscope. T = tendon 42
5.29 Modulus as a function of depth at the interface for an AM sample. Green line is resin. Method: Displacement control with increased DSC 42
5.30 Value of the mean modulus between 700 and 1000 nm for indents at the interface, in an AM sample. Color scale unit is GPa. T = tendon, B = bone 43
5.31 The curves represent 4 different typical tests: load control and displacement control for bone and load control and displacement control for tendon. 43

5.32 Modulus as a function of depth in the bone for a DIO sample. Green line is resin. Method: Load control 44
5.33 Value of the mean modulus between 100 and 200 nm for indents in the bone, in a DIO sample. Color scale unit is GPa. B = bone 44

List of Tables

4.1 Parameters for μCT scans. V = voltage, I = current, VS = voxel size, FSS = focal spot size, TM = tube mode, ET = exposure time, ST = scan time, # images = number of images per sample 12
4.2 Parameters for CE-CT scans. V = voltage, I = current, VS = voxel size, FSS = focal spot size, TM = tube mode, ET = exposure time, ST = scan time, # images = number of images per sample 13

5.1 Pre-polishing steps 28
5.2 Polishing steps 28
5.3 Parameters for nanoindentation experiments. DSC = detection stiffness criteria . 31

List of abbreviations

AGE	Advanced glycation end-product
AM	Age-matched
CE-CT	Contrast-enhanced computed tomography
CSM	Continuous stiffness measurement
DCM	Dynamic contact module
DIC	Differential interference contrast
DIO	Diet-induced obesity
DSC	Detection stiffness criteria
MF	Mineralized fibrocartilage
NMF	Non mineralized fibrocartilage
PBS	Phosphate-buffered saline solution
POM	Polyoxymetalate
ROI	Region of interest
SEM	Scanning electron microscopy
T2DM	Type 2 diabetes mellitus
VOI	Volume of interest
μCT	X-ray microfocus computed tomography

Chapter 1

Introduction

The role of the musculoskeletal system is to support and stabilize the human body and coordinate the movements of the muscles and the skeletal system. It is composed of bone, muscle, cartilage, tendon, ligament, and other connective tissues. Tendons are joined to bone in a specific way to form the insertion site, also known as the enthesis, or bone-tendon interface, to facilitate joint motion [6]. The tissue that makes up this interface between tendon and bone is a complex transitional tissue, which is essential for physiologic musculoskeletal motion. It serves to integrate and minimize stress concentrations between two distinct tissue types : the bone which is a stiff, structural hard tissue and the tendon which is a compliant structural soft tissue. Hence, the elastic modulus of bone is much larger than that of tendon. Therefore, the role of the interface is to make these two different tissues function in unison.

Because of its function of mediating load between very dissimilar tissues, the bone-tendon interface is a common site of injury. The problem is that, in case of such injury, the natural tissue is not regenerated after healing. Instead, it is replaced with a so-called scar tissue, which is isotropic and significantly less stiff than either tendon or bone. It has been reported that depending on the severity and the location of the injury, the regenerated tissue will fail in 20 to 94% of cases [5].

A solution to this problem would be to regenerate the tissue using a construct composed of a scaffold (made of a biomaterial) with growth factor and/or cells to obtain a tissue that presents the same properties as the original one. For the replacement of biological tissue, it is necessary to first understand the characteristics of the tissue to be replaced, knowing that these properties can also differ depending on age or disease/pathology. However, this critical junction is poorly understood because it has been understudied due to the difficulty to find appropriate testing methods that can examine 3D properties at a relatively small scale. As a matter of fact, the interface averages 100 μm to 1 mm in length depending on the species and age [7]. In this context, the purpose of this thesis is to characterize the bone-tendon interface at the level of the Achilles tendon-to-heel bone insertion both regarding its 3D compositional and structural characteristics and its mechanical properties. The influence of age and type 2 diabetes are also studied. To achieve this, two high resolution techniques are used: X-ray microfocus computed tomography and nanoindentation.

In order to complete these objectives, this thesis is organized in several chapters. First, chapter 2 describes what is known up until today about the bone-tendon interface and its characterization methods. Then, chapter 3 describes the problem and states the objectives of the thesis. In chapter 4, all the experiments and results that are related to the structural and compositional characterization of the bone-tendon interface are presented. Chapter 5 is dedicated to the characterization of the mechanical properties of the interface. Finally, chapter 6 contains a general discussion, some future perspectives and concludes the thesis.

Chapter 2

State of the art

This chapter starts by giving a review of the structure and composition of the bone-tendon interface as described in the literature, followed by a description of the influence of age and diabetes on its properties. Finally, an overview of the currently applied characterization methods is given.

2.1 Structure and composition of the interface

An abrupt transition between bone and tendon would lead to stress concentrations and risk of failure. That is why a tissue, called the bone-tendon interface, is present to make the transition between these two very different materials. The tendon-to-bone insertion site can be classified according to the type of tissue that it is made of: dense fibrous connective tissue or fibrocartilage. In the first case, the tendon attaches to the bone via fibrous tissue (similar to tendon in structure) while in the case of fibrocartilaginous tissue, the tendon attaches to the bone through a layer of fibrocartilage. The majority of insertion sites in the body are fibrocartilaginous and these are also the most frequently injured [6]. The shoulder's rotator cuff tendon-to-bone attachment, for example, one that has significant clinical relevance because of its high chances of injury and high failure rate for reattachment (94%), is a fibrocartilaginous transition [8]. The insertion that is studied in this work is the Achilles tendon-to-bone insertion, which is also a fibrocartilaginous insertion and an important one as it provides an enormous amount of mobility for locomotion.

According to literature, the enthesis can be divided into four specific discrete zones with varying compositional and mechanical properties and functions [2] :

1. The first one is the fibrous tendon, containing 90% volume of aligned collagen fibers of type I with small amounts of decorin, which is a proteoglycan, and the remaining volume is water. The structure of the tendon is hierarchical : the smallest unit is the triple-helix collagen molecule which accumulates in groups of five to form microfibrils. These in turn aggregate to form fibrils, followed by fibers, and fascicles. The last ones combine to form the final structure of the tendon. The diameter of the collagen molecule is 1.5 nm and the diameter of the tendon is of the order of magnitude of a few millimeters in human [2].

2. The second zone is the non mineralized or uncalcified fibrocartilage, which is composed of collagen of types II and III and only small amounts of types I, IX, and X and of decorin and aggrecan (cartilage-specific proteoglycan) [2].

3. The third zone is composed of mineralized or calcified fibrocartilage containing mainly type II collagen and some type X collagen and aggrecan [2]. It contains chondrocytes which are bound in lacunae. They confer limited repair capabilities to the fibrocartilage because, as a result of the lacunae, the chondrocytes cannot migrate to damaged areas.

4. The last zone is the bone. It is composed of approximately 40% in volume type I collagen with the same hierarchical structure as tendon and more or less 50% volume of apatite which is a stiff phosphate mineral. Residing in this matrix are osteoclasts, osteocytes, and osteoblasts [2].

Figure 2.1 is a representation of the anatomy of the Achilles tendon-to-bone insertion with its four regions, as just described.

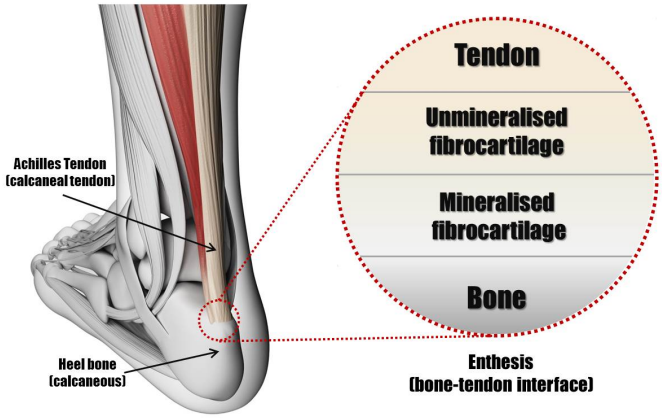


Figure 2.1: The anatomy of the bone-tendon interface [4].

Some studies go even further by describing that, through these four regions, there is a gradual change in some of the compositional and structural properties to further decrease stress concentrations. This can be seen on the left drawing of figure 2.2. Indeed, a gradient in the concentration of mineralization and in the orientation of the collagen fibers across the bone-tendon interface has been observed. The gradation in mineral content is represented by the blue shading, the bone being mineralized and represented in blue and the tendon is not mineralized (white). This was measured using Raman spectroscopy in [2]. The gradation in fiber orientation is represented by the lines, going from an orthotropic orientation in tendon to an isotropic orientation in bone. This was measured using polarized light microscopy, also in [2]. It is crucial to remember that these measurements have been done in 2D; hence it has not been proven that these gradients exist in 3D as well.

When an injury occurs at the bone-tendon interface, surgery is performed but chances of retear are very high because the body is unable to regenerate the original tissue on its own. Studies describe that in the naturally regenerated tissue, there is no more gradient in mineralization and there is a sudden change in the orientation of the collagen fibers. The right scheme of figure 2.2 represents this regenerated tissue, showing the abrupt change is mineralization and in fiber orientation. The native tissue is thus extremely hard to recreate because of its complex biological and mechanical properties and its specific composition. This proves the complexity in finding an optimal healing strategy of the bone-tendon insertion site.

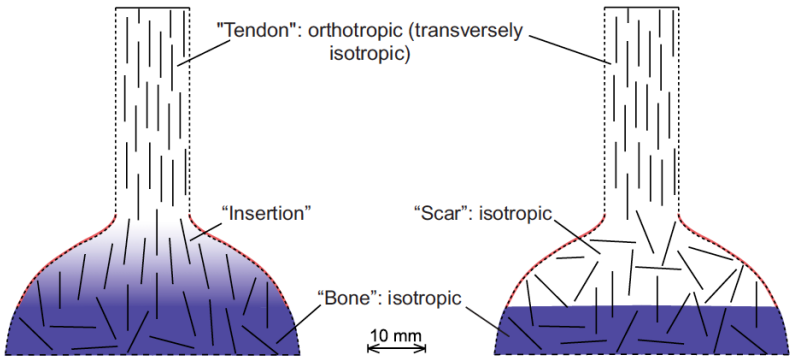


Figure 2.2: Model of the natural bone-tendon interface (left) and bone-tendon interface after healing (right) for the human supraspinatus insertion [5].

However, in another study [7], they analyzed the insertion site of the anterior cruciate ligament and bone in the knee joint to study the interface mineral presence and distribution. To do this, they used energy dispersive x-ray analysis and backscattered scanning electron microscopy. They obtained results that are in contradiction with what was described previously: they detected mineral presence only in the third zone (mineralized fibrocartilage) and in the bone region. Their images revealed a sharp transition instead of a gradient in mineral content between zones 2 and 3.

2.2 Effect of ageing on bone-tendon interface

Almost no data is available on the effect of ageing on the interface. It was, however, studied in [9]. They analyzed the changes in matrix composition and organization of the anterior cruciate ligament in the knee in different age groups of a bovine model. They found differences in the collagen fiber orientation for the groups by looking at them under polarized light: in younger groups, a near 90° bend in collagen fiber orientation was observed near the interface region (collagen fibers being parallel to the interface), while in the older group, the collagen fibers were perpendicular to the interface. Mineralization was found to be age-dependent as well. The degree of mineralization increased with age. This was studied under light microscopy using Von Kossa staining. However, no mineral was detected in the ligament nor in the uncalcified fibrocartilage zone of the interface. They observed a sharp transition between mineralized and non-mineralized regions and this was the same for all age groups.

This study, however, refers to a different animal model and a different body region from the one considered here.

2.3 Effect of type 2 diabetes on bone-tendon interface

Type 2 diabetes mellitus (T2DM), the most common type of diabetes, is a life-long disease with a growing prevalence. Here, the focus will lie on high-fat diet induced obesity driven T2DM, which is caused by a lack of physical activity and a high caloric diet leading to obesity and characterized by insulin resistance[1] in the liver and peripheral tissues and a defective insulin secretion from pancreatic beta cells leading to hyperglyceamia (high blood glucose levels). When hyperglycaemia becomes chronic, it can result in microvascular complications such a nephropathy,

[1]Insulin produced by the pancreas is not able to break down the glucose that is present in the bloodstream and store it in the body cells, glucose builds up in the bloodstream and causes damage to the body and in the mean time the cells can not function properly without receiving glucose.

neuropathy, and retinopathy or macrovascular complications such as coronary heart disease, peripheral arterial disease, and stroke, which in turn increase mortality rate. During the past years, treatment for T2DM patients has improved and mortality rate has decreased significantly. However, with this increase in life expectancy, other side effects of diabetes have started to appear such as weakened bones or thickening of the tendons and ligaments of hands and feet [10]. For example, it has been reported that the soft tissue of the Achilles tendon is significantly thickened in individuals with diabetes [11]. They associated the thickening of the tendon to two causes: first the non-enzymatic glycation of the collagenous component due to hyperglycaemia in diabetic patients and, second, due to the increase in the mechanical load on the foot resulting from the higher body mass in diabetic people. When T2DM is accompanied by neuropathy, it can also include symptoms like reduced strength in the ankle muscles. Recent evidence suggests that T2DM may also cause alterations in collagen structure, such as irregular fibril morphology and density, accumulation of AGEs (Advanced Glycation Endproducts) which could play a role in the mechanical function of tendons. Results showed that stiffness, but not modulus, is significantly reduced in the Achilles tendon [12]. Regarding the mineralization degree, it has been shown [13] that mean calcium concentration in bone is more elevated and that mineralization heterogeneity is lower in individuals with T2DM.

2.4 Available methods for characterization

This section will describe the currently applied testing methods for the structural and mechanical characterization of the bone-tendon interface (or bone and tendon separately) with their pros and cons.

Structural characterization

In [2], they characterized the supraspinatus tendon-to-bone insertion by looking at the gradation in mineral concentration and the collagen fiber orientation. Mineral concentration was determined using Raman spectroscopy, which allows to investigate the degree of mineralization on a micro-scale level in a non-destructive way. Polarized light microscopy was used to measure collagen fiber orientation. Using this technique, they were able to analyze sections of the tissue. This, however, only gives 2D information on the orientation of the fibers.

Other techniques to evaluate mineral presence and distribution include: energy dispersive x-ray analysis (EDAX), backscattered scanning electron microscopy (SEM), and Fourier transform infrared spectroscopic imaging (FTIR-I). The first two were used in [7]. EDAX allows to obtain the elemental composition profiles of specific regions. For example, calcium and phosphorous peaks will appear for mineralized regions. This technique is advantageous to get a quantitative measure of mineral presence. In SEM images, mineral content can be observed because elements with higher atomic number, such as calcium and phosphorous are represented by brighter areas. FTIR-I was used in [14] and is a sensitive imaging modality that is capable of mapping the matrix composition and distribution of a relatively large sample area.

X-ray microfocus computed tomography or μCT is an imaging technique that can be used to characterize the structural arrangement of tissues. It consists in using the same principle as is used in hospital CT scanners but on a small scale with increased resolution. It has been used to obtain high resolution 3D information at the microscopic level. It is a non-destructive technique, returning the sample intact and it does not require sample preparation. However, one of its main drawbacks, is that soft tissues such as muscles and tendons can hardly be distinguished because of their low absorption coefficient. Mineralized tissues, on the contrary, can be well visualized as they absorb x-rays much better. In [10], they used μCT to characterize the structural alterations

of the cortical and trabecular bone in an obesity-driven type 2 diabetes mouse model. They were able to observe, with high resolution, the trabecular architecture and cortical macrostructure and porosity of the tibia. μCT was also used in [15] to observe the structure arrangement of the periodontal ligament (PDL) and blood vessels. In order to observe these structures, their specimens were stained overnight with phosphotungstic acid. In [16], they used μCT to obtain two dimensional sagittal plane images of the humerus and supraspinatus tendons together with histomorphometry to determine the gradient slope in mineralization content and the length of the gradient region. In order to do this, they used a soft tissue threshold to distinguish unmineralized and mineralized tissue from background.

Contrast-enhanced CT (CE-CT) is a technique in which samples are stained with a contrast agent before performing μCT in order to visualize tissues with different absorption coefficients, resolving the problem of traditional μCT. This is a powerful technique that is convenient to analyze the bone-tendon interface as it allows to see both tendon and bone simultaneously. It has advantages compared to classical histology because it does not require extensive sample preparation. Moreover, histology is often limited by the sectioning orientation of the sample and the depth resolution. CE-CT can be used for 3D quantitative imaging of mineralized and soft tissue. However, the challenge is to find the optimal contrast agent that will bind well to the tissue without altering or affecting its properties. Multiple contrast agents have been proposed in literature. Lugol's iodine solution has been used as a contrast agent for μCT imaging of small invertebrates, vertebrate embryos, and certain isolated parts of larger, post-embryonic vertebrates [17]. Promising results have been obtained with this agent. The drawback is that Lugol dehydrates the sample. Another contrast agent, called polyoxometalate (POM), has been developed by the KU Leuven. This one is not invasive as it does not dehydrate the sample. It is a novel chemical compound for CE-CT that allows simultaneous three dimensional multi-tissue visualization and characterization [18]. POM-based CE-CT has been shown [18] to be able to provide a detailed 3D representation of the structural organization of the mineralized bone and bone marrow vasculature and adipose tissue. It has also been shown [18] that POM-based-CE-CT is able to show clear differences during ageing and diet-induced obesity in these tissues. Hafnium-substituted Wels Dawson POM is a possible POM formulation which is known to be stable under physiological pH and temperature. It is used in the form of a salt. Results of Hf-POM-based CE-CT have been shown to be strongly correlated to histology. One drawback of POM is that it does not allow to see collagen fibers as well as Lugol does.

Mechanical characterization

Another important step in studying the bone-tendon interface is characterizing its mechanical properties. As biological tissues have a non-elastic behavior, there is a need for proper mechanical testing methodologies, set-ups and protocols. Interface mechanical properties have been studied in [7] by coupling uniaxial microcompression with optimized digital image correlation (DIC) analysis. DIC can track the location and displacement of texture patterns with surface markers to deduce surface deformation. It is a high resolution method that allowed them to obtain stress-strain profiles and elastic moduli of the interface regions. However, DIC has also some drawbacks: it is a 2D method that is only able to measure on the surface of the samples

Nanoindentation has also been used for characterizing mechanical properties of small samples. It is a mechanical test that consists in measuring the depth of an indenter tip into a material in function of the applied load. It has been used to map the elastic modulus of non natural heterogeneous materials, such as ceramic composites or metal grains [19]. It has also been used more recently, to examine biological materials. It is a tool that provides high resolution, it allows to examine properties in different directions, and it can be used to characterize complicated local mechanical properties of materials. All of these advantages are beneficial for applications in

biological tissues [20]. A drawback of nanoindentation, though, is that the sample preparation is very difficult for biological tissues. This is because it requires a perfectly flat surface, which is easy to obtain for materials such as metals, but very challenging for biological samples, especially for soft tissues. Another drawback of nanoindentation is the extensive time required to map a surface. A few studies have performed nanoindentation to determine mechanical properties at the bone-tendon or bone-ligament interface. In [20], nanoindentation was used to investigate the transition from non mineralized to mineralized fibrocartilage in the knee anterior and posterior meniscal insertions of humans. They found an increase in the instantaneous elastic modulus when going from non mineralized fibrocartilage to mineralized fibrocartilage to bone. An advantage of this study is that they used human tissues which are bigger than most animal tissues used in other studies. In [21], they used two-directional nanoindentation on mineralized turkey leg tendon to investigate the extent of elastic anisotropy in this tissue. In this study, however, they did not measure properties at the bone-tendon interface, only in the tendon. AFM-based nanoindentation was used by [15] and [22] to measure the elastic modulus for the human bone-PDL insertion and PDL-cememtum insertion (attachment between tooth and bone). They investigated the causes for narrowing of the PDL-space which included higher values of elastic modulus for both insertions.

Chapter 3

Problem statement and objectives

3.1 Problem statement

As has been mentioned before, the bone-tendon interface is a site that is prone to injury. Unfortunately, very often the healed tissue does not have the same properties as the original one. Hence, the final objective is to replace the original bone-tendon interface with a new engineered tissue that will have the closest properties to the original one as possible. However, a critical step in any regeneration or tissue engineering effort is a highly detailed determination of the properties of the tissue to be replaced, as well as improving the understanding of diseases involving this tissue. That is why, developing an understanding of the tissue's structure, composition, and function is a prerequisite for interface regeneration.

In previous studies, only information in two dimensions is available on the changes in mineral content and fiber orientation (e.g. using histology, microscopy or spectroscopy). Using a technique that provides data in three dimensions will give more accurate and detailed information on these properties.

For determining the mechanical properties, there is a lack of information on nanoindentation studies, even though, nanoindentation is a powerful technique that can determine mechanical properties of a small, heterogeneous material at a nano-scale resolution, which is exactly what is required for the characterization of the interface.

3.2 Objectives of the thesis

The purpose of this thesis is to characterize the Achilles tendon-to-heel bone insertion in 3 dimensions. In short, this is done by analyzing the structural properties through X-ray microfocus computed tomography (μCT) and contrast-enhanced μCT (CE-CT), and the mechanical properties thanks to nanoindentation. Additionally, the effect of ageing and T2DM are studied. Indeed, little is known about the effect of ageing on this tissue. Therefore, the goal is to find out if there is an evolution with age on the properties of the interface. Also, very little is known about the effect of diabetes on the properties of the bone-tendon interface. As said before, diabetes is a disease with a growing prevalence, known to affect bone and tendon properties. This makes it an interesting research topic.

The first objective of this thesis involves the characterization of the interface thanks to 3D high-resolution μCT. More specifically, the differences in mineralization in the different zones of the interface are studied. Then, the focus is laid on the mineralized fibrocartilage of the interface in order to study its physical properties and compare them between groups.

The second objective is to use μCT on contrast-enhanced samples to study the structural properties such as collagen fiber orientation. It is crucial to improve the interpretation of CE-CT data. Indeed, being able to interpret data and scans correctly and draw the proper conclusions is an important step for this technique, as CE-CT has not been used in the past for studying fiber orientation on these kinds of samples. A comparison is also made made between the different groups.

The third objective involves the use of nanoindentation in order to analyze the changes in mechanical properties across the bone-tendon interface. However, as nanoindentation is a recent method for mechanical characterization of biological tissues, a crucial step in the frame of this work is to optimize the protocol for sample preparation and the testing parameters, which is challenging for micrometer-scale sized samples with heterogeneous properties. Therefore, focus lies on the methodology for preparing and testing the samples.

Chapter 4

X-ray microfocus computed tomography

4.1 Principle of μCT

4.1.1 Components

The most important elements that compose a μCT system include an X-ray source, a turntable on which the sample is placed, an X-ray detector, and a computer [23]. Figure 4.1 shows the general set-up of a μCT device.

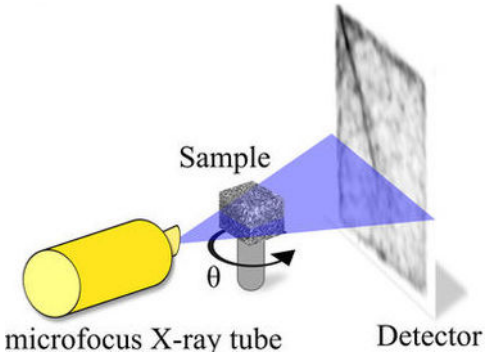


Figure 4.1: General set-up of a μCT system

1. The **x-ray source** is mainly composed of a cathode and an anode. The cathode consists of a thin filament and acts as the source of electrons. The anode serves as the target and is usually made of tungsten. The electrons are created in the form of a thin beam at the cathode thanks to a high voltage electrical current and are then accelerated from the cathode to the anode thanks to a high voltage power source that is connected between them. With a target material that is thin enough, and electrons with high enough energy, X-ray photons are transmitted through the target.

2. The **x-ray detector** makes use of a scintillating material. When electrons hit this material, they produce flashes of light that are counted. The detector is composed of a charged-coupled device (CCD) camera, an image intensifier, and a scaling down medium. The image intensifier converts x-rays to light photons. The CCD camera is sensitive to visible light, it counts the number of electrons released by each pixel. Finally, the scaling down medium is used because of the size difference between the light emitting material and the CCD chip.

4.1.2 Acquisition

A certain amount of X-rays are absorbed by the object, depending on its density and the atomic number of the atoms composing the object. Multiple 2D images, called radiographs, from different angles are formed when X-rays hit the object while it rotates and are captured by the detector to form a 3D representation.

Important parameters for image acquisition include the number of radiographs that are taken and the signal-acquisition time per radiograph. The rotation of the object is usually 180° but can also be 360° for irregularly shaped objects. The detector can be put closer or further away from the source to decrease or increase the spatial resolution. Each point that has been recorded corresponds to a sinusoidal curve (sinogram). These sinograms then have to be converted into a 3D stack of 2D images.

4.1.3 CE-CT

CE-CT is used for the visualization of the tendon. For this method, the samples have to be treated before scanning with a contrast agent that contains an attenuating element. For the purpose of this study, Lugol's iodine solution is used to stain the samples. Indeed, in the past, Lugol has shown to be a good contrast agent for the visualization of collagen fibers, which is an important factor in this case.

4.2 Materials and methods

4.2.1 Animal samples

The Achilles tendon-to-bone interface was extracted from 18 mice: six 8-week-old mice (Young), six 30-week-old mice (called AM for age-matched) and six 30-week-old mice with obesity-induced type 2 diabetes (called DIO for diet-induced obesity). To induce obesity-driven T2DM, mice were fed on a high fat diet for 22 weeks, developing obesity, hyperglycaemia and insulin resistance. All the samples were fixed in 4% paraformaldehyde during 16 hours and then stored at 4° C in a phosphate-buffered saline solution (PBS). Next, the samples were dissected in order to isolate the tendon and the bone and remove all tissue that was unnecessary for the purpose of the experiments. Figure 4.2 shows the approximate size of a dissected sample. The bone-tendon interface itself is approximately 200 μm long.

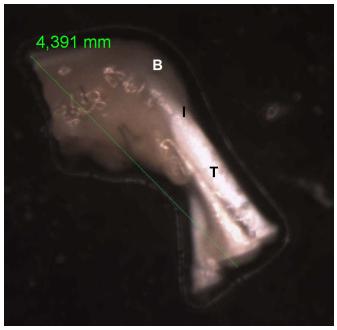


Figure 4.2: Light microscopy of a typical dissected and cleaned muring Achilles bone-tendon sample. The white part in the lower right part of the figure is the Achilles tendon (indicated by T), the darker part in the upper part of the image is the heel bone (indicated by B). I indicates the interface

4.2.2 Sample preparation

Very little sample preparation is required before doing μCT. The samples were wrapped into parafilm and placed inside the μCT chamber and adjusted so that they were positioned at the correct height.

For CE-CT, the samples were placed in a PBS solution containing 30 % of Lugol for 3 days to stain them before performing μCT on them. They were then, just like for the previous scans, wrapped in parafilm before starting the scanning.

All the samples were scanned with μCT (18 samples), only half of the samples (three from each group) were scanned with CE-CT. Because these samples needed to be stained, they could not further be used after CE-CT. The other half of the samples was kept intact to use them for nanoindentation.

4.2.3 μCT image acquisition

For the experiments, a Phoenix Nanotom® m - nanoCT® Computed Tomography System (GE Sensing & Inspection Technologies GmbH, Wunstorf, Germany) was used (see figure 4.3). It has a 3072x2400 pixels detector, a 180kV/15W energy nanofocus X-ray tube.



Figure 4.3: The Phoenix Nanotom® m

CT parameters The parameters used for the μCT scans, prior to staining, can be found in table 4.1. The aluminium filter has a thickness of 0.2 mm.

Table 4.1: Parameters for μCT scans. V = voltage, I = current, VS = voxel size, FSS = focal spot size, TM = tube mode, ET = exposure time, ST = scan time, # images = number of images per sample

V(kV)	I (μA)	VS (μm)	FSS (μm)	TM	skip	average	filter	ET (ms)	ST (min)	# images	target
60	87	1.25	1.24	0	0	1	Al	500	20	2400	tungsten

CE-CT parameters The parameters used for the CE-CT scans can be found in table 4.2. In this case, the aluminium filter also has a thickness of 0.2 mm.

Table 4.2: Parameters for CE-CT scans. V = voltage, I = current, VS = voxel size, FSS = focal spot size, TM = tube mode, ET = exposure time, ST = scan time, # images = number of images per sample

V(kV)	I (μA)	VS (μm)	FSS (μm)	TM	skip	average	filter	ET (ms)	ST	# images	target
60	87	1.25	1.24	0	1	3	Al	500	1h12min25s	2100	tungsten/diamond

4.2.4 μCT and CE-CT image analysis

Three softwares were used for analysis and visualization of the data from the μCT scans. CTAn (Bruker MicroCT, Kontich, Belgium) enables to visualize data and select regions of interest (ROI). ROIs can be drawn on multiple slices and the software can interpolate these ROIs to all slices of a selected dataset. This allows to obtain a 3D volume of interest (VOI). CTAn, then, allows to further process the VOI to analyze different parameters like, for example, the structural thickness, volume, surface, porosity, etc.

For data visualization, DataViewer and CTvox (Bruker MicroCT, Kontich, Belgium) were used. DataViewer allows for 2D and 3D visualization through three different views (coronal, transverse and sagittal) for all slices, and allows to do 3D image registration. CTVox allows to visualize a selected VOI in 3D.

Once the high resolution μCT images, prior to staining, were obtained, they were analyzed thanks to the CTAn software. More specifically, the mineralized fibrocartilage (MF) was examined. The MF is the porous region of the interface that can be observed in the μCT scans (see blue region in figure 4.4). As there was a very large amount of images per sample, first a selection of images had to be made. Most of the images did not contain any information, hence, about 400 images were selected for each sample. Next, an ROI was drawn manually on about every 10 to 20 images out of the 400 (figure 4.4). The CTAn software then interpolates the ROI to the images where it has not been drawn. All the ROI's from the images of one sample form a VOI. Next, the images were binarised using automatic Otsu segmentation, followed by a closing operation with a squared kernel of radius 2 to remove noise and fill small pores. Then, using 3D analysis, the mean thickness (μm), the maximum thickness (μm), and the total volume (μm^3) of the VOI, and hence the MF layer, could be computed. Then, using manual global segmentation, the images were binarised for the pores and this allowed to compute the number of pores and the pore density ($\#/mm^3$) for each sample.

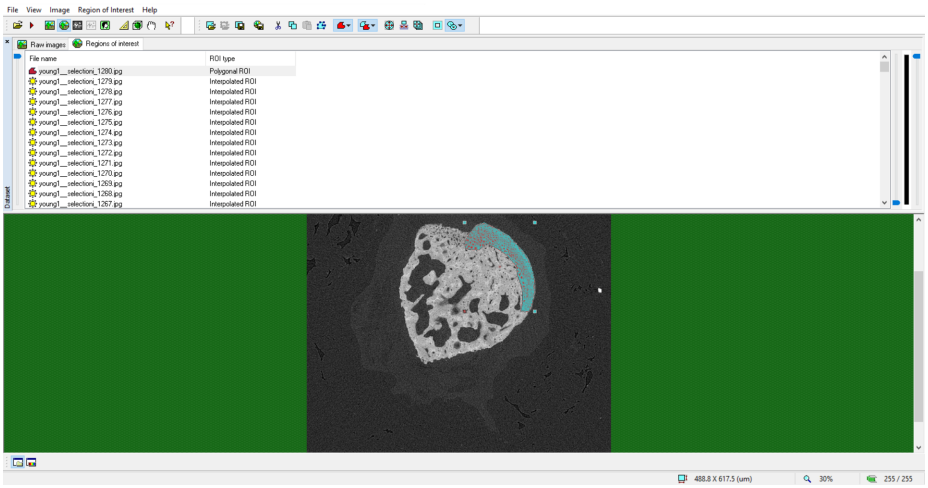


Figure 4.4: Screenshot of CTAn software showing an ROI, indicated in blue, drawn on a transverse image of a dataset obtained from a young mouse sample

After the VOI was obtained for each sample, the contact length between the MF and the non mineralized fibrocartilage (NMF) (μm) was measured for all samples. This length was measured manually on every 10 images images of a data set and the mean was taken for all images of each sample. Figure 4.5 shows how the contact length was measured on one ROI image.

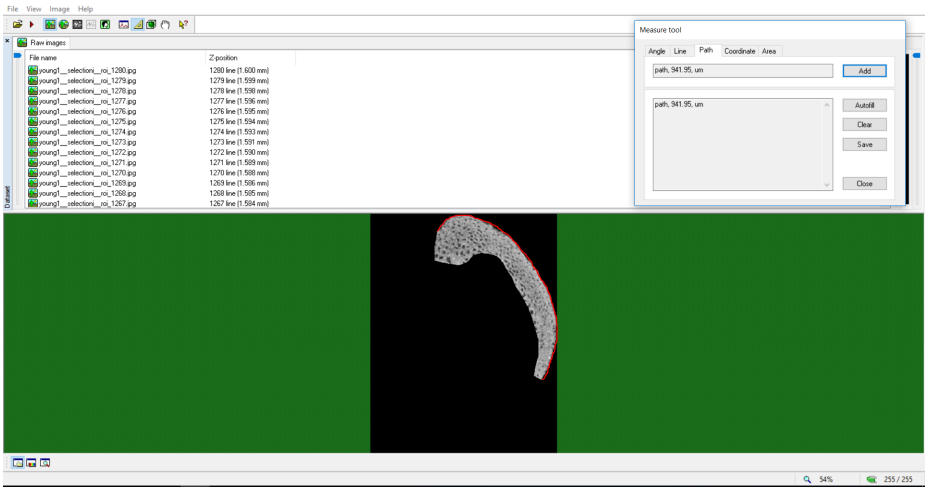


Figure 4.5: Screenshot of CTAn software showing how the contact length was measured for one ROI image obtained from a young mouse sample, the red line is the contact length

Next, the thickness of the tendon (μm) was measured on the CE-CT scans, this could, of course, be done only on half of the samples, which were stained and scanned again. So, the mean was taken for the 3 samples of each group. This was done manually using the DataViewer software. The thickness of the tendon was measured at the same location for all samples, close to the interface.

Finally, the CE-CT scans were also used to visually study the collagen fiber orientation in the different groups.

4.2.5 Statistical analysis

All parameters (mean and maximum thickness, volume, number of pores, and pore density of the MF, contact length between MF and NMF, and tendon thickness) were computed for all groups (Young, AM, and DIO). For all sets of data, normality tests were performed thanks to the Shapiro-Wilk normality test. The presence of outliers was tested using the Dixon test. Mean $\pm$ standard deviation (SD) were computed for each group. F-tests were performed to check for the equality of variances between groups ($p > 0.05$ means no significant difference in variance). A two-tailed, unpaired t-test with equal or unequal variance depending on the result of the F-test was done to compare means ($p<0.05$ means that there is a significant difference between means). t-tests could only be performed between Young and AM samples (difference in age, both healthy) and between AM and DIO samples (same age, difference in health) because there is only one parameter changing between these groups. Young and DIO could not be compared statistically because there are 2 parameters varying between these groups.

For all the bar graphs, when a significant difference between groups was observed for $p<0.05$, it is represented by one star (*), for $p<0.01$ by two stars (**), and for $p<0.001$ by three stars (***).

4.3 Results and discussion

This section will describe and discuss the results that were obtained, studying the μCT and CE-CT scans as was explained in the previous section.

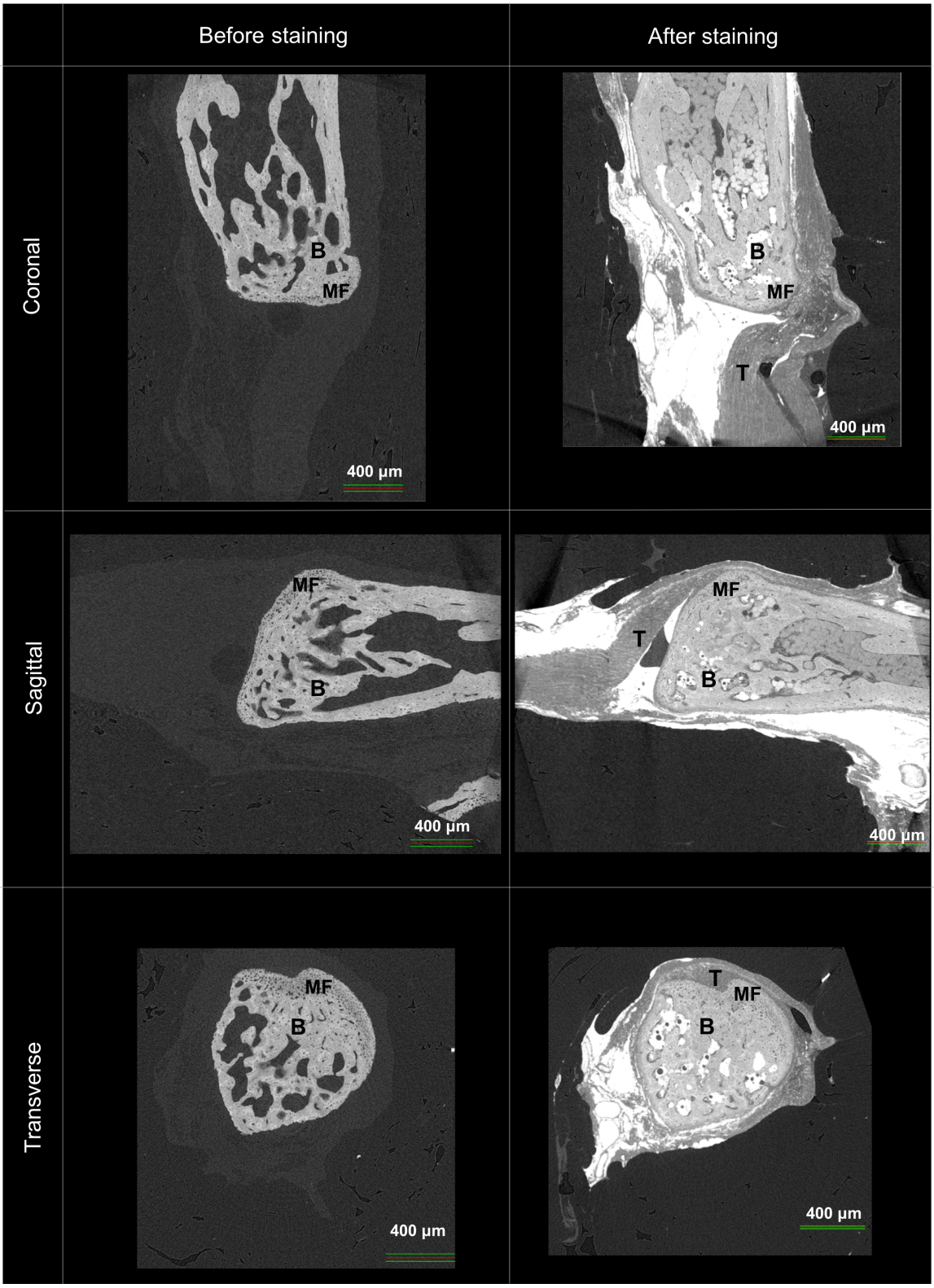


Figure 4.6: Coronal, sagittal and transverse views from μCT scans before and after staining (CE-CT) for a young mouse sample. B is bone, T is tendon and MF is mineralized fibrocartilage.

Figure 4.6 displays the results that were obtained for a young mouse sample. For a general overview, a comparison is made between the scans before and after staining (CE-CT) for three different views (coronal, sagittal and transverse). It can be seen that the bone and MF (porous region) and visible on all images. The tendon can be visualized only on the scans after staining, which is their purpose. The four different regions of the interface can thus be visualized on the CE-CT scans: the bone, MF, NMF, and tendon. However, it is more difficult to distinguish the boundary between NMF and tendon. The next part of this section will be split in two: first the results from the scans before staining (μCT) will be presented and discussed, followed by the results and discussion from the scans after staining (CE-CT).

4.3.1 μCT

As was described in the State of the art chapter, two gradients are described in literature for the enthesis, one in the content of mineralization and one in the orientation of the collagen fibers. The content in mineralization will be discussed here while collagen fiber orientation will be discussed with the CE-CT results.

The presence of a gradient in mineralization going from tendon (which is not mineralized) to bone (which is mineralized) means that there should be a gradient in the grayscale, on the images, especially those before staining. Indeed, after staining, images might not show the lower amounts of mineralization because of the staining of the soft tissues. By looking at the results, however, the bone and the MF are clearly visible but it does not seem that there is a gradient in grayscale. It looks like there is a clear and sharp transition between these two regions. The same holds for the transition between MF and NMF. This can be seen on figure 4.7, which is a close-up coming from the upper-left scan shown in figure 4.6, meaning for a young sample. The same is, however, true for the two other groups. Figures 4.8 and 4.9 show the interface before staining for an AM and a DIO sample, respectively. Again, the separation between regions is sharp and not gradual. These results agree with the results obtained in [7], mentioned in the State of the art. The bone and the MF are clearly mineralized, while the NMF and the tendon are not. There is a clear transition in mineralization instead of a gradient in mineralization content.

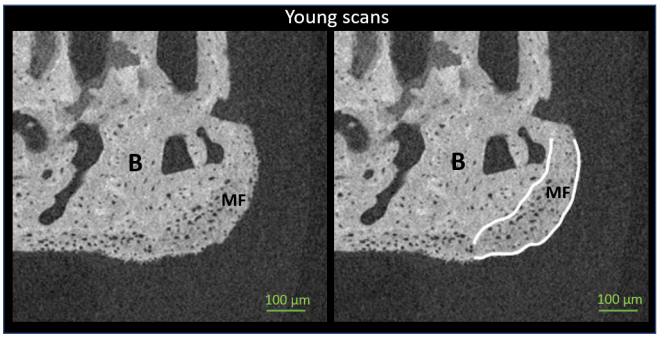


Figure 4.7: Left: Close-up view of the interface of a young sample. Right: same image showing the clear separation between regions

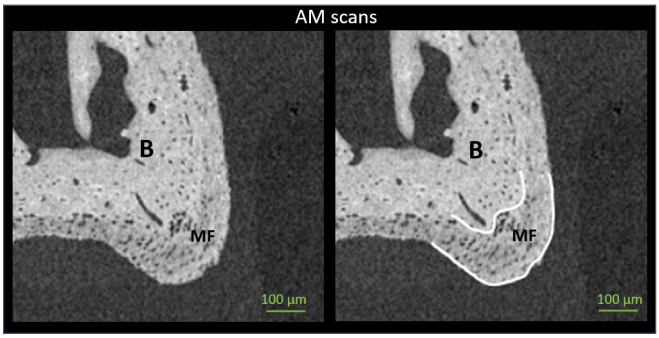


Figure 4.8: Left: Close-up view of the interface of an AM sample. Right: same image showing the clear separation between regions

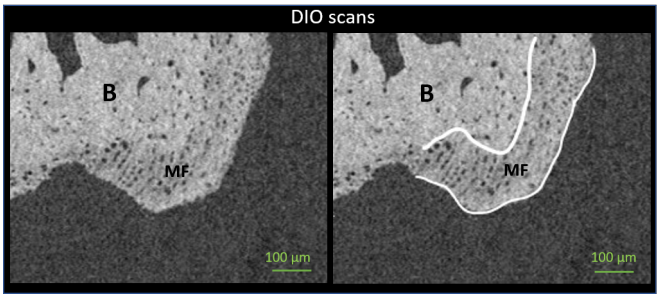


Figure 4.9: Left: Close-up view of the interface of a DIO sample. Right: same image showing the clear separation between regions

Next, the MF region was studied more in details, also on the original μCT scans, with the CTAn software. A 3D representation of this region can be observed in figure 4.10, obtained with the CTVox software. This gives an idea of what the MF looks like in 3D.

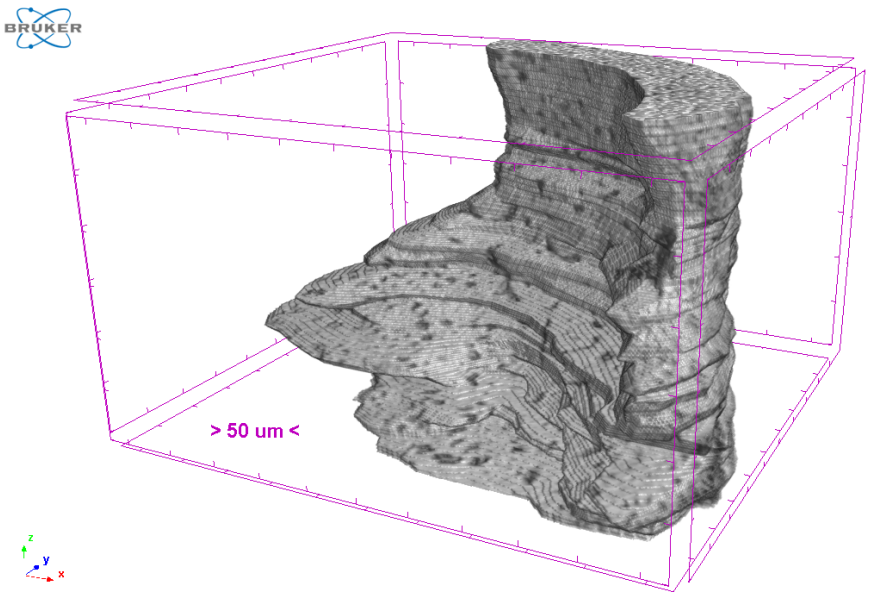


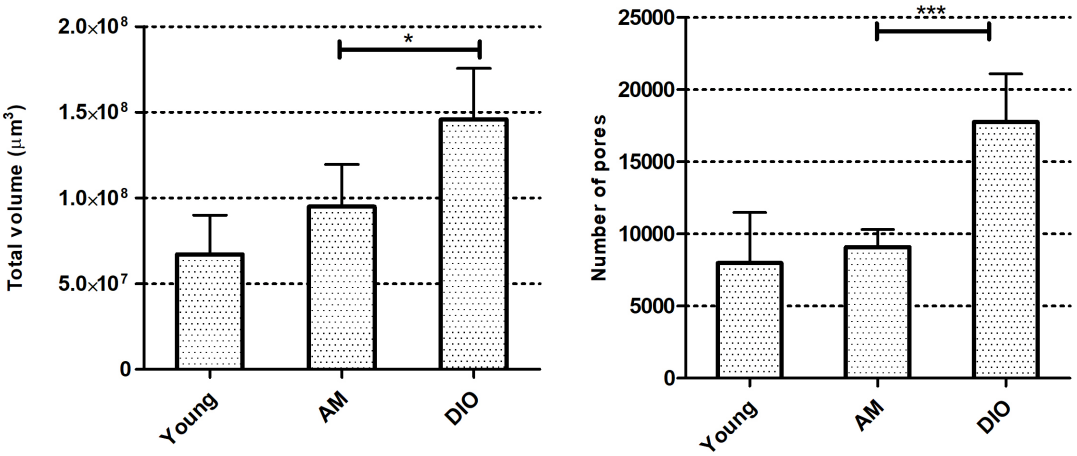
Figure 4.10: The MF (VOI) computed with the CTAn software and represented in 3D with the CTVox software

In this region, the volume, number of pores, and thickness were studied for all samples. The

contact length between the MF and NMF was measured on the ROIs.

First, the total volume of the MF was averaged for all three groups (figure 4.11a). The mean and standard deviation for all the samples from each group are represented on the bar graph. It can be seen that the volume of the MF increases from Young to AM and to DIO samples. However, the volume difference between Young and AM samples is not significant while the volume difference between AM and DIO is significant (p=0.012).

Next, the number of pores in the MF was examined for the three groups (figure 4.11b). It can be seen that there is an increase in number of pores from Young to AM to DIO but there is no significant difference between the number of pores of Young and AM samples while there is a significant increase in the number of pores for the DIO samples (p=0.000039).



(a) Total volume of the MF

(b) Total number of pores in the MF

Figure 4.11: Graphs comparing differences in volume and in number of pores of the MF in the three groups

From these results, it can be hypothesized that the increase in the number of pores could be related to the increase in volume. To verify this, the number of pores was normalized with the volume to obtain the pore density. The hypothesis was confirmed and this can be seen on the graph in figure 4.12. The number of pores per unit of volume is approximately equal for all groups:

- Young: $120 \cdot 10^3$ pores/mm^3
- AM: $100 \cdot 10^3$ pores/mm^3
- DIO: $124 \cdot 10^3$ pores/mm^3

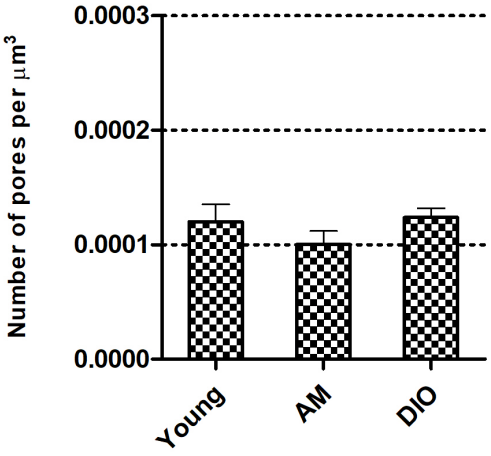


Figure 4.12: Graph comparing the pore density in the MF for all groups

The next parameters that were studied were the mean and the maximum thickness of the MF. No significant differences were observed for these two parameters (see figure 4.13). The mean and maximum thickness are larger for DIO samples but this is not significant.

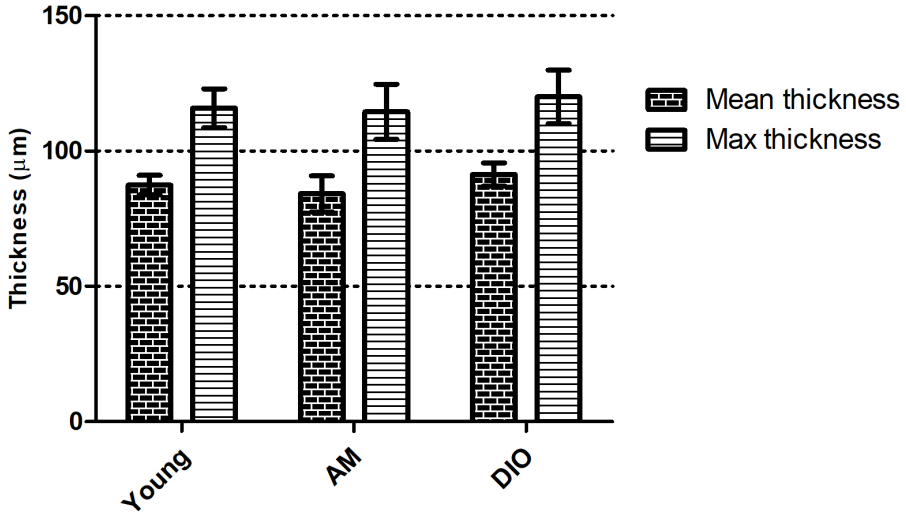


Figure 4.13: Graph comparing the mean and maximum thickness of the MF for all groups

It was found that there is a significant difference in the volume of the MF between AM and DIO groups, but no significant difference in the thickness of the MF between AM and DIO groups. This means, if not the thickness, there should be another dimension of the MF that induces the difference in volume. This is why the contact length between MF and NMF was studied. Indeed, if this length is larger it could mean that instead of the thickness of the MF it could be its width that is larger, inducing an increase in volume of the MF for DIO samples. The results can be observed in the graph in figure 4.14. It shows that there is indeed a significant difference ($p=0.048$) in the interface contact length between AM and DIO groups.

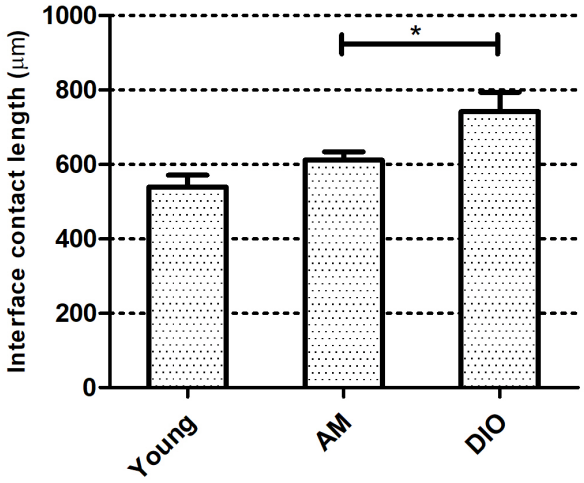


Figure 4.14: Graph comparing the length of the interface between MF and NMF for all groups

With the previous results, we know that, with ageing, the dimensions of the MF did not significantly change, while there is a clear increase in the volume of the MF and in the contact length between the MF and NMF for DIO mice.

Several causes could explain these results. First, the increased volume of the MF in diabetic models can be explained by a biological effect called chondrogenesis, which is the process by which cartilage is developed. Second, the increase in volume can also be explained by the physical effect, called mechanobiology. These two causes will now be discussed in more details.

Chondrogenesis is the earliest phase of skeletal development and the process by which cartilage is developed. However, it has been shown in [24] and by *in vitro* experiments on fracture healing (personal communication with Carlos Marin, PhD student of Prof. G. Kerckhofs) that there is a delay in the process of chondrogenesis in diabetic mice. This was discovered thanks to results showing that fracture healing is slower for individuals with diabetes. The delay in chondrogenesis is explained by diminished chondrogenic gene expression. Consequently, a larger volume of cartilage in diabetic models could be explained by a delay in bone formation.

Mechanobiology studies how physical forces and changes in the mechanical properties of cells and tissues contribute to development, cell differentiation, physiology, and disease. A major branch of this field is the study of the mechanisms by which cells respond to mechanical loads. There is, for example, a relationship between bone formation and the mechanical environment the bone is subjected to. When strains are below the physiological threshold, bone is resorbed, while when strains exceed the upper boundary of the physiological domain, bone is formed. Normally, in healthy adults, bone is in homeostasis because osteoblasts form new bone while osteoclasts resorb existing bone. After a fracture, bone healing is also subject to mechanical regulation [25]. As the weight of the DIO mice was significantly increased, this induced a larger effective mechanical load on their skeleton. This could, in turn, cause the increase in volume of the MF. To summarize, in the case of mechanobiology, the increase in volume is attributable to the increase in body mass commonly observed in diabetic patients rather than to DM itself.

4.3.2 CE-CT

In the previous section, it was found that there was an increase in the contact length between the MF and NMF. This could possibly be explained by an increase in the thickness of the tendon but could not be verified on the μCT scans. To verify this, it is necessary to use the CE-CT scans where the tendon can be visualized. The tendon thickness was measured manually on the images. It is important to note, however, that there are only 9 samples instead of 18 for the previous cases. As can be seen, on the graph in figure 4.15, there is an increase of the thickness from AM to DIO, even though, the difference is not significant (p = 0.058).

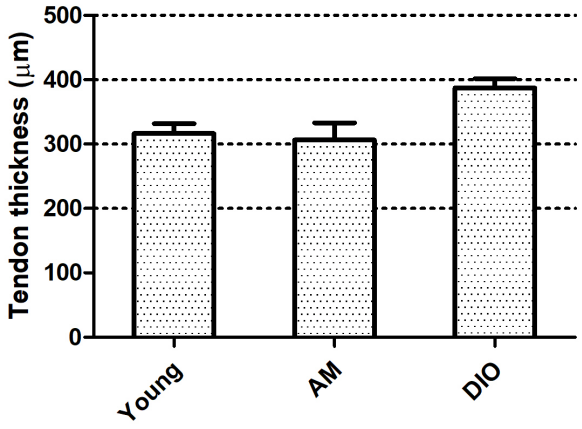


Figure 4.15: Graph comparing the thickness of the tendon for all groups

The increase in the tendon thickness can be correlated with the results that were obtained in [11]. Indeed, as was mentioned in the State of the art, they described a thickening of the tendon in individuals with diabetes, explained by two causes: mechanobiology and the non-enzymatic glycation of collagen which is caused by hyperglycaemia (high blood glucose levels) in diabetic models due to insulin resistance.

Mechanobiology was already discussed previously, together with the increase in volume of the MF. As was mentioned, the body mass of the DIO mice was significantly increased, this induced a larger effective mechanical load on the foot and partly explains the increase in the thickness of the Achilles tendon.

The other reason that explains the thickening of the tendon is non-enzymatic glycation. Indeed, hyperglycaemia leads to the non-enzymatic glycation [1] of the collagenous component leading in turn to structural changes. Glycation, in the end, results in the formation of advanced glycated end products (AGEs), which is an irreversible process leading to various complications in diabetes, including thickening of the tendon. AGEs can also induce cross-linking of collagen, which contributes to the rigidity and the loss of elasticity of tissues, and to the thickening of capillary walls observed in diabetes. Stiffening of the tendon can thus also be observed.

In this next part, the orientation of the collagen fibers will be discussed. Figures 4.16, 4.17, and 4.18 demonstrate the orientation of the fibers on the stained scans for three different samples from the three different groups, Young, AM, and DIO, respectively. On the left side of each figure, a coronal view is displayed and on the right side, a sagittal view can be observed. For every view, there is also an enlarged image (white box) of the bone-tendon interface, highlighting

[1] process by which glucose is chemically bound to amino groups of proteins without the help of enzymes

the fiber orientation. The fibers have been drawn manually for clarity.

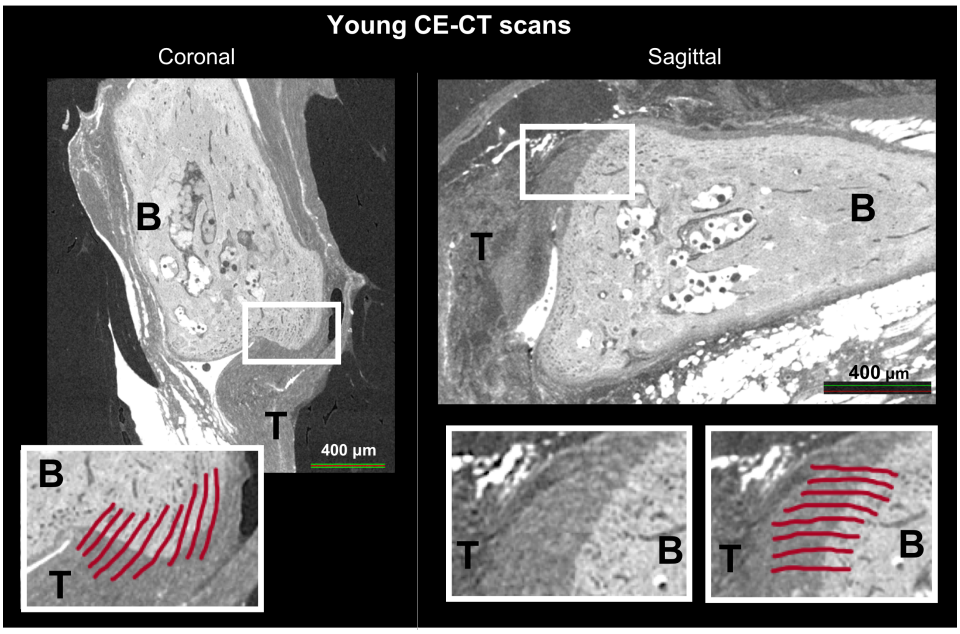


Figure 4.16: Coronal and sagittal views of fiber orientation for Young sample with a zoom on the bone-tendon interface. T = tendon, B = bone

Looking at figure 4.16, which displays CE-CT scans for a young sample, it is clear that in the tendon, the fibers are nicely aligned. At the level of the interface, the perfect alignment of the fibers is continued, perpendicular to the interface, into the MF. Where the bone region starts, the alignment of the fibers is not visible anymore.

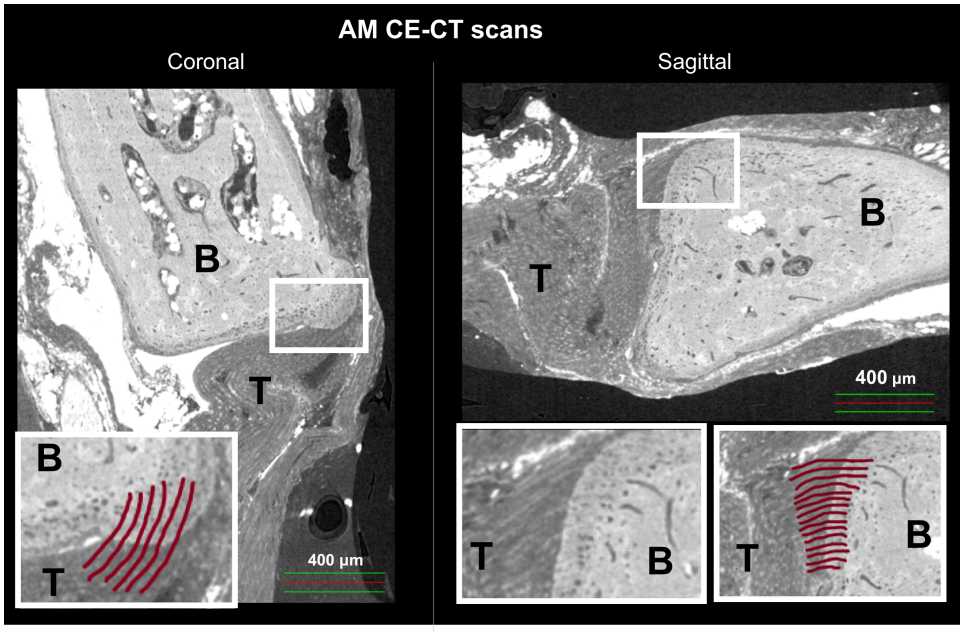


Figure 4.17: Coronal and sagittal views of fiber orientation for AM sample with a zoom on the bone-tendon interface. T = tendon, B = bone

For the AM sample in figure 4.17, the same can be observed as for the young sample, fibers

are well aligned in the tendon and continue to be this way at the interface, again perpendicular to the interface. Once the bone starts, the fibers are not visible anymore. This differs from the results that were obtained in the study mentioned in the state of the art [9] where they mention that collagen fibers are parallel to the interface in younger groups as opposed to older groups where the fibers are perpendicular to the interface. However, they also found that there are differences in fiber orientation between different insertions: the femoral and tibial insertions. Fibers are much more aligned in the tibial insertion while being much less organized at the femoral insertion. This indicates that there could be differences in the fiber orientation for the Achilles tendon-to-bone insertion as well compared to the femoral and tibial insertions.

On the DIO scans in figure 4.18, the fiber alignment is not visible at the interface. It is, however, visible in the tendon. This can be seen by looking at the orange box, showing a close-up of the tendon for the coronal view. The separation at the interface for a DIO sample also seems to be less sharp and clear than for the 2 other groups.

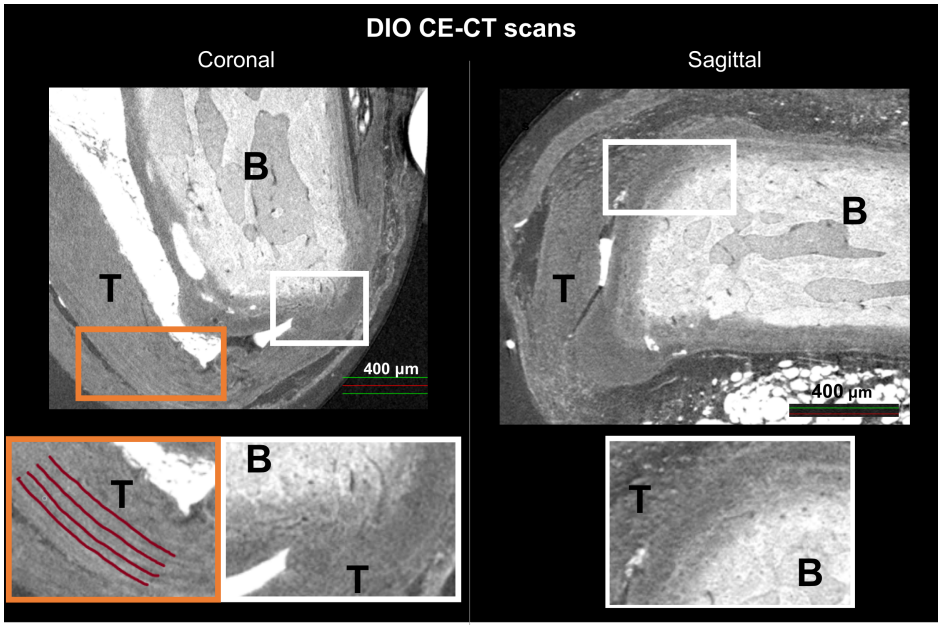


Figure 4.18: Coronal and sagittal views of fiber orientation for DIO sample with a zoom on the bone-tendon interface and on the tendon. T = tendon, B = bone

In order to further analyze this, figure 4.19 makes a comparison before and after staining for a DIO sample. It is interesting to see that, when looking at the scan before staining, the orientation of the fibers is actually visible in the MF, just like it was on the scans after staining for the young and AM samples. However, of course, the NMF and the tendon are not visible at the interface before staining, so the orientation of the fibers there cannot be seen. This phenomenon could be linked to the cross-linking of collagen that is induced by AGEs in DIO models as was mentioned before but this is not certain and surely needs further investigation in order to determine the exact cause.



Figure 4.19: Comparison before and after staining of a DIO sample, highlighting fiber orientation in the MF

4.4 Conclusion

The results from this first part on μCT and CE-CT have shown that it is possible to obtain highly detailed information on the structure of the bone-tendon interface with this non-invasive technique, requiring very little sample preparation.

Results showed that for all samples, there was a sharp transition at the interface instead of a gradation in mineralization, the bone and mineralized fibrocartilage being mineralized while the tendon and non mineralized fibrocartilage are not.

Thanks to the μCT image analysis, it was possible to study the MF of the bone-tendon interface. Analysis of the MF revealed an increase in volume from young to aged to DIO samples, the increase being only significant for DIO samples. This was explained through biological and physical effects: a delay in chondrogenesis and mechanobiology. The pore density of the MF was found to be equal for all groups, as well as the MF thickness. There was a significant increase in the contact length of the MF with the NMF for DIO samples compared to the age-matched ones, which explains the increase in volume of the MF but also the increase in thickness of the tendon for MF. This increase in thickness of the tendon was explained by two factors: mechanobiology and non-enzymatic glycation of collagen fibers.

Regarding fiber orientation, for all three groups, fibers were visible and well aligned in the tendon. For young and aged groups, this well structured alignment of the fibers continued at the interface up to the MF, as could be seen in the scans after staining. Then, there was a sharp transition with the bone, where the fibers were not visible. They are still present in bone but are not aligned and thus much harder to distinguish. For diabetic samples, this fiber alignment was visible in the tendon but not at the interface. To visualize the fiber alignment at the interface, it was necessary to look at the scans before staining, which showed perfect alignment of the fibers in the MF but obviously could not show the prolongation of the alignment of the fibers in the tendon. It was hypothesized that the fact that the fibers are not nicely visible at the interface as in other groups could be linked to cross-linking of collagen fibers in diabetic models but further investigation is needed to confirm this and to find other potential causes for this phenomenon.

Chapter 5

Nanoindentation

5.1 Principle of nanoindentation

Nanoindentation consists in applying a certain load to a surface to induce local surface deformation. During loading and unloading, the load and displacement are monitored, allowing to obtain a displacement versus load graph, which in turn allows to determine properties such as the reduced modulus and the hardness of a given material. A load is applied with a tip which is often made of diamond and has a spherical or pyramidal shape to prevent its deformation. Thanks to its small probe size, nanoindentation has become an essential tool for determining the local mechanical properties of small, thin, heterogeneous materials, with a submicron resolution. Figure 5.1 shows a typical load-displacement curve for quasi-static indentation in metals and ceramics. For these materials, which are assumed elastic, isotropic, and with negligible adhesion, the compliance method can be applied to compute the hardness H and the elastic modulus E, two important parameters for nanoindentation. The hardness can be computed as

$$H = \frac{P_{max}}{A}$$

where P_{max} is the maximum load and A is the projected contact area between the indenter tip and the sample at maximum load. The reduced elastic modulus E_r is the combined modulus of the tip and the sample and is computed as:

$$E_r = \frac{1}{\beta}\frac{S}{2}\frac{\pi}{\sqrt{A}}$$

where S is the initial unloading stiffness (the slope of the unloading curve dP/dh, evaluated at the maximum load) and β is a geometrical constant equal to 1. The reduced modulus E_r and the elastic modulus E are related by:

$$\frac{1}{E_r} = \frac{1-\nu_i^2}{E_i} + \frac{1-\nu_s^2}{E_s}$$

where the subscript i refers to the indenter material, and subscript s refers to the substrate material, and ν is Poisson's ratio. For the nanoindenter that was used in the present work, $E_i = 1141$GPa and $\nu_i = 0.07$

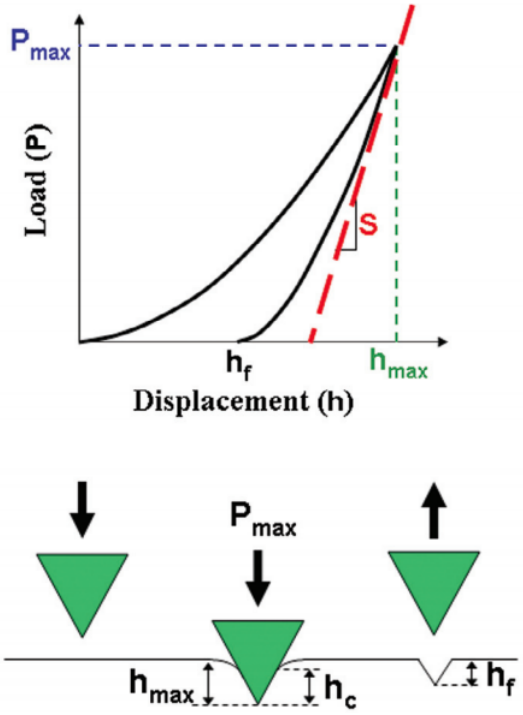


Figure 5.1: Typical load-displacement curve and indentation process [3]

Of course, biological materials are viscoelastic, exhibiting time-dependent behavior. The main effect of viscoelasticity on indentation is creep, which means that the tip continues sinking into the sample even under constant load. When loading is followed directly by unloading without a hold at maximum load, displacement increases slightly in the initial part of the unloading phase, because the creep rate of the material is initially higher than the imposed unloading rate. With this phenomenon, it is impossible to use the compliance method described above, because a negative slope is observed in the initial unloading region. To eliminate this effect, it has been found [26] that instead of doing loading and unloading without a hold between them, a hold period should be incorporated at peak load in order to allow the material to approach equilibrium before the unloading. This makes it possible to use the formulas listed above (from the compliance method) and was always done for all tests.

5.2 Materials and methods

5.2.1 Nanoindenter

The nanoindenter that was used is the *Agilent Nano Indenter G200* and is shown in figure 5.2. It is equipped with a nanoindention tip but also with an optical microscope (magnification x10 or x40) to visualize and analyze the surface of the sample before and after indentation. It is provided with a sample tray which can contain four samples at most at four different locations and in the middle of these four locations, there is a sample made of silica which serves as a reference for adjusting the height of the other test samples and for calibrating the tip height. All this together is placed inside a box which is closed during testing in order to minimize the effects of exterior acoustic vibrations. Usually, a batch of tests is pre-programmed during the day and the tests themselves are performed during the night to even further minimize exterior disturbances (from people moving in the room, for example). Each single indent lasts for about 5 to 8 minutes and the indenter tip pauses for about 30 minutes before starting in a different zone (in the same sample or in another sample) in order for the tip to stabilize. With the nanoindenter, a software (*KeySight NanoSuite*) is provided which allows to control the nanoindenter and extract

and analyze the results. This software has to know the exact distance between the sample and the indenter tip after the sample has been focused under the microscope. The software also allows to move along the surface of the sample and record the exact coordinates of a certain spot on the sample. The software allows to pre-program a series of tests having each their own pre-defined parameters and containing a selected number of indents. The nanoindenter can be used with different heads. The standard configuration uses the XP indentation head, which delivers < 0.01 nm displacement resolution and > 500 μm maximum indentation depth. The indenter can also be equipped with the Dynamic Contact Module (DCM) head which is a sensitive head. It allows to extend the range of load-displacement experimentation to the surface contact level. It is a fully dynamic indentation head for ultra-low-load (10 mN maximum load) mechanical properties characterization. The Continuous Stiffness Measurement (CSM) mode is compatible with both the XP and the DCM heads. It corresponds to the oscillation of the tip at a certain frequency during loading. This allows to obtain several measures of the modulus and the hardness in function of displacement. It satisfies application requirements that must take into account dynamic effects, such as strain rate and frequency. It is important to note that this nanoindenter measures, time, load and stiffness very well. However, the indentation depth is a less reliable measure.

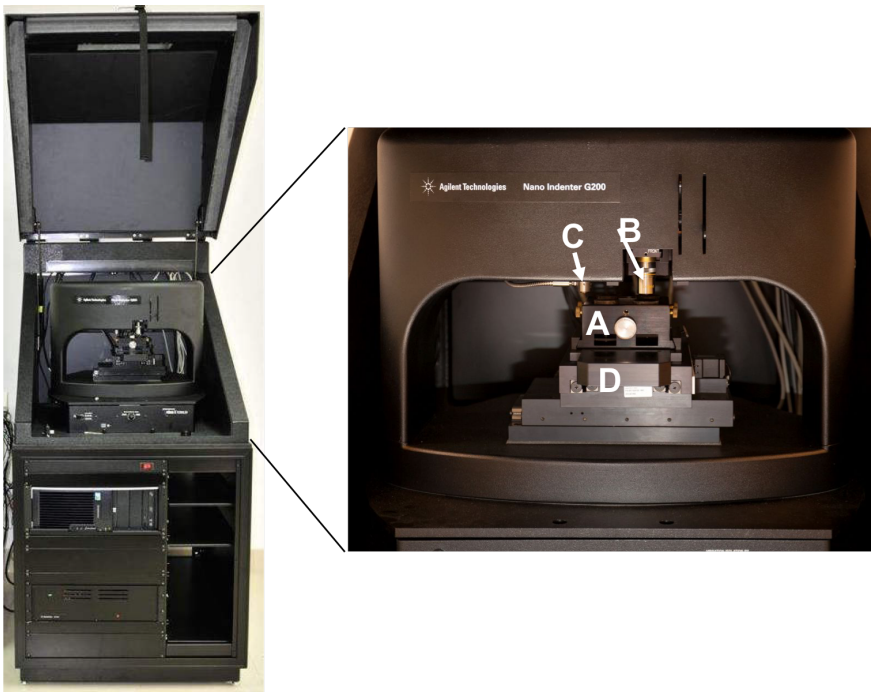


Figure 5.2: The *Agilent Nano Indenter G200*. A = sample tray, B = microscope, C = indentation tip, D = moving platform

An important factor when performing mechanical tests is the state of the sample. It is important to notice that in the frame of this work, the samples that have been used were fixed in paraformaldehyde before nanoindentation. This was absolutely necessary in order to keep the samples in good shape for a considerate amount of time. It is crucial to keep in mind, however, that the mechanical properties that were measured can be and and are probably affected by the chemical fixation.

A second important factor is the hydration state of the sample tissue. Dehydration removes the water present in the tissue. Studies have been performed with dehydrated tissue to reduce viscoelasticity and to bring the modulus to the optimal range for performing indentation [27].

Other studies have been performed on hydrated tissue [20]. Dehydrated and hydrated tissue may act in very different manners and the modulus may differ widely from one state to the other. In the frame of this study, tests have been tried in both conditions and this will be further explained in the next chapter.

5.2.2 Sample preparation

To perform nanoindentation, the samples first had to be prepared. The goal was to obtain a surface that could be indented and that contained the tendon as well as the bone, placed in the correct way so that the interface between them was also visible. The requirements were to obtain a surface that was as flat and horizontal as possible and which was not too thin (at least 5 μm thick) so that the tip could measure correctly. Nine samples were destined for nanoindentation (the three from each group that were not used for CE-CT). This task was quite challenging because of the small size and the heterogeneity of the samples. Different experimental protocols had to be tested as described below. All sample preparation trials were done on testing samples.

Method A: Epoxy resin embedding and polishing (1)

The sample was embedded in epoxy resin. To do this, it was placed on the bottom of a mold with the help of a metal clip (spring) and the resin was poured over it in the mold. After 24 hours of drying, the sample was taken out of the mold. The surface then had to be prepared for nanoindentation. At the lab, a protocol had already been set up for bone alone. This same protocol was tested. Surface preparation consisted in pre-polishing and then polishing of the sample as described in the two following tables:

Table 5.1: Pre-polishing steps

Step number	**1**	**2**	**3**
Support	SiC paper	SiC paper	SiC paper
Abrasive	SiC	SiC	SiC
Grain size	320	1200	4000
Lubricant	Water	Water	Water
Rotation speed(rpm)	150-200	150-200	150-200
Time (min)	Roughly straighten out surface	01:00	02:00

Table 5.2: Polishing steps

Step number	**1**	**2**
Support	MD-Mol	MD-Nap
Abrasive	DP-Spray	DP-Spray
Grain size	$3\mu m$	$1\mu m$
Lubricant	DP-Lubricant Blue	DP-Lubricant Blue
Rotation speed (rpm)	150	150
Time (min)	03:30	01:30

MD-Mol and MD-Nap refer to *Struers* polishing cloths. DP-Spray refers to *Struers* spray containing exclusively polycrystalline diamonds, sprayed on the cloth before polishing. DP-Lubricant blue refers to *Struers* alcohol-based lubricant for polishing.

Method B: Epoxy resin embedding and polishing (2)

For this method, the sample was attached to a metal support thanks to 2-sided tape. A drop of epoxy resin was placed on the sample under vacuum (figure 5.3). After 24 hours of drying, the embedded sample could be removed from the metal support thanks to alcohol. The tape was removed as well.

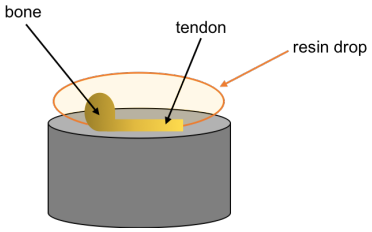


Figure 5.3: Scheme of sample preparation for nanoindentation (step 1) - Method B

The drop of resin, containing the sample, could be turned around and placed on another support to perform nanoindentation (figure 5.4).

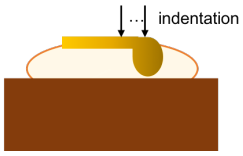


Figure 5.4: Scheme of sample preparation for nanoindentation (step 2) - Method B

Some polishing still needed to be performed but this was minor compared to the previous trial. Only step 2 of polishing was needed (see table 5.2).

Method C: Cryomatrix resin embedding and cryostat sectioning

The third approach was performed in a different lab because it involved the use of a cryostat (*Leica CM3050 S*), a device used to make frozen sections. Cryomatrix embedding resin was poured in a small mold and the sample was positioned inside the resin, more resin was poured over the sample and the mold was then placed in ice for 15 to 20 minutes so that the resin could harden. Once this was done, the sample was removed from the mold and placed in the cryostat chamber which was kept at a temperature of -24°C. Once the sample had been placed in the chamber, it could still be oriented for sectioning. Different thicknesses of slices could be cut ranging from 25 μm up to 200 μm. These slices were then placed on glass slides.

Method D: Epoxy resin embedding and microtome sectioning

The fourth and last approach involved the use of a microtome (*Leica EM UC6*). First, the sample was further dissected under a microscope in order to make it as small as possible while still keeping the bone-tendon interface intact. Then, the sample was dehydrated with ethanol for one hour and a half. Next, epoxy resin (made of a mix of 2.5 g of epoxy resin an 0.3 g of hardener) was made. After one hour and a half, the resin had started to polymerize and the sample was placed inside a very small mold (much smaller than the ones mentioned for the previous trials) and the resin was poured over the sample. Because the resin had partly polymerized, and had become a bit more viscous, it was easier to keep the sample from moving (no adhesive had to be used to hold it). After 24 hours the embedded sample was removed from the mold. The objective was then to cut thin sections from the sample with the microtome to obtain flat slices. The thickness of these

slices was of less than 1 μm. Each slice was placed on a glass slide and adhered to it thanks to a drop of water. Two surfaces could be tested with nanoindentation: the slice on the glass slide or the remaining sample embedded in the resin. The slice on the glass slide was too thin to be indented as the nanoindenter requires a thickness of at least 5 μm. The remaining embedded sample was thus kept for nanoindentation. However, before doing that, the remaining of the embedded sample was placed back in the mold and resin was poured again on top of the sample. This was done so that the resin would fill all the pores and gaps that were present in the bone and in the tendon. A few sections were again cut from the sample after the resin had dried and this allowed to obtain a flat surface without pores, which is an ideal surface for nanoindentation. For the entire process, a glass blade was used for rough sectioning while a diamond blade (*DiAtome Histo Cryo*, 45° angle, section thickness range 0.2-5 μm) was used for the fine cutting, these last blades are very expensive compared to glass blades and were only used when strictly necessary.

Figure 5.5 is a rough sketch (top view) explaining sample preparation for method D and how nanoindentation should be performed on the sample afterwards in the different regions of the sample (bone, interface, and tendon).

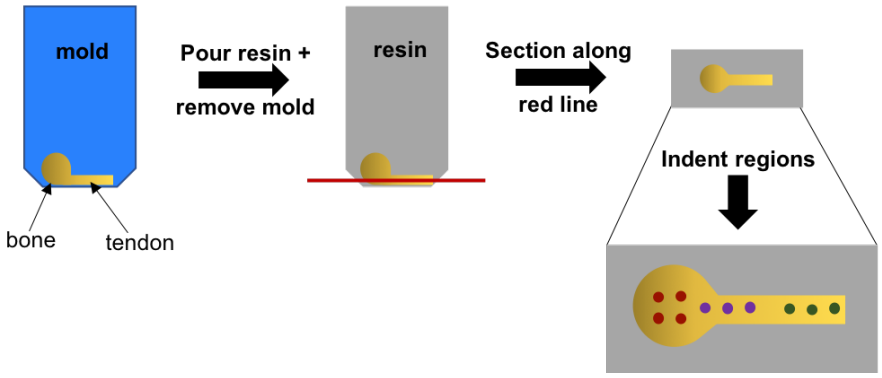


Figure 5.5: Scheme of sample preparation and nanoindentation, as seen from the top - Method D

5.2.3 Testing parameters

Table 5.3 contains the list of parameters that were used for nanoindentation. Most of the tests were performed using the parameters in the first column ("Displacement control"), with a stopping criteria in terms of depth set to 1000 nm. As some problems were observed with surface detection, two other methods were tested later, only on 4 out of the 9 good samples and not on the test samples during sample preparation testing. The second one ("Displacement control with increased DSC"), uses the same parameters as the first one, except that the initial distance between the tip and the surface was set to 10 μm instead of 1 μm, this allowed to increase the surface approaching speed and set the surface detection stiffness criteria more sensitive. The last approach ("Load control") consisted in changing the stopping criteria to load instead of distance. In this way, the surface detection stiffness criteria could be set "very sensitive". Then, if the indenter "thought" it had detected the surface but was actually still in the air, it would continue anyways because the stopping criteria was expressed in terms of load and set to 1mN. This was tested with the same surface approach distance and surface approach velocity as in "Displacement control with increased DSC".

Table 5.3: Parameters for nanoindentation experiments. DSC = detection stiffness criteria

Parameter	Displacement control	Displacement control with increased DSC	Load control
Tip	Berkovich	Berkovich	Berkovich
Method	XP head with CSM method	XP head with CSM method	XP head with CSM method
Surface approach distance (nm)	1000	10 000	10 000
Surface approach velocity (nm/s)	10	50	50
Surface DSC (N/m)	100 (Sensitive)	50 (Very sensitive)	25 (Ultra sensitive)
Strain rate (s^{-1})	0.05	0.05	0.05
Harmonic displacement (nm)	2	2	2
Frequency (Hz)	45	45	45
Depth limit (nm)	1000	1000	-
Max load (mN)	-	-	1

Because the modulus is computed based on Poisson's ratio, this value also needed to be given to the nanoindenter for the materials that were used. According to literature, Poisson's ratio for bone is equal to 0.3 [28] while Poisson's ratio for tendon is equal to 0.5 [29] and was kept equal to 0.5 through the interface. All indents in a same region were always placed 20 μm away from each other in both x and y directions.

5.3 Results and discussion

5.3.1 Optimization of the sample preparation

This section will present the results that were obtained for the different sample preparation methods and which one was chosen for performing nanoindentation. This step was crucial and had to be performed on test samples.

Method A: Epoxy resin embedding and polishing (1)

The results of method A were rather unsatisfactory. Many bubbles and impurities entered the resin during polishing and it was challenging to polish without damaging the sample. The result can be seen in the scanning electron microscopy (SEM) image of figure 5.6. The tendon and bone can very hardly be identified. They probably have been ripped apart due to the polishing and a lot of artifacts can be observed, such as air bubbles in the resin.

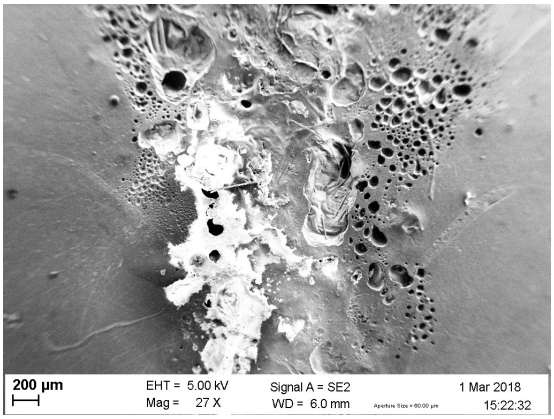


Figure 5.6: SEM image of embedded and polished sample - Method A

Method B: Epoxy resin embedding and polishing (2)

The results of the second sample preparation method can be observed in the SEM image of figure 5.7. Here again, parts of tendon and bone have been ripped apart. Pieces of bone can be distinguished along the right side of the image. The tendon is on the left side of the picture but it has mostly been destroyed during polishing.

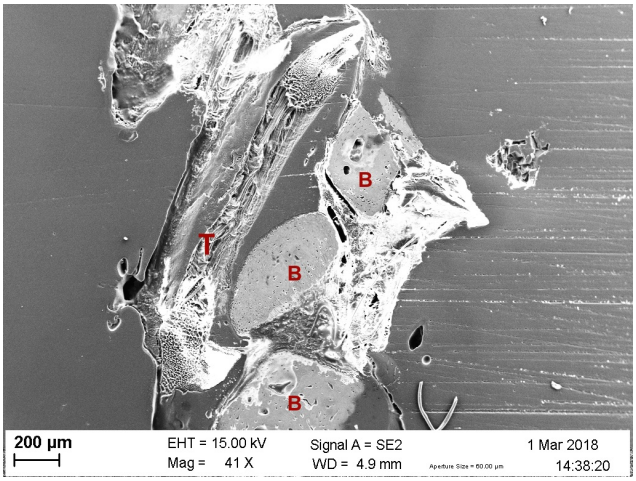
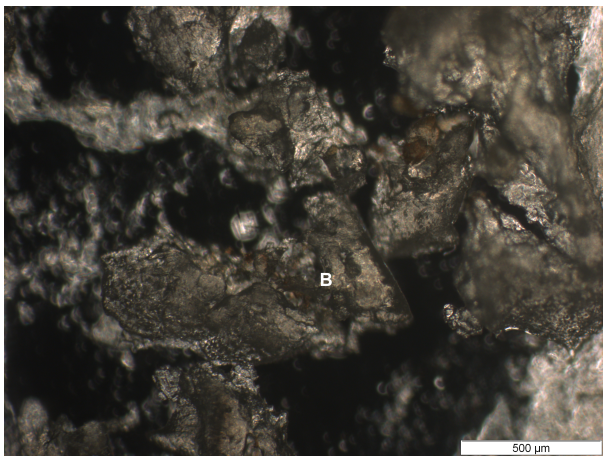


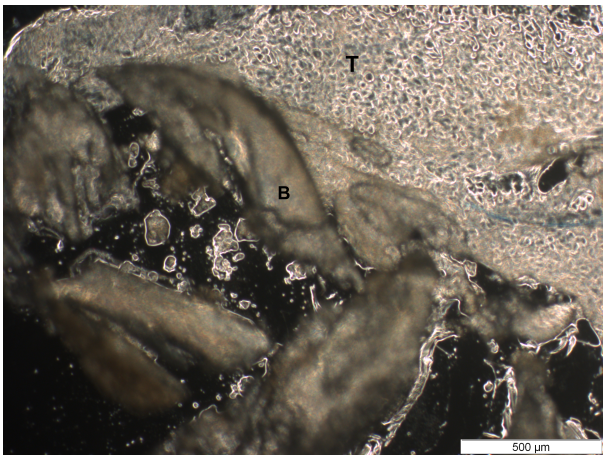
Figure 5.7: SEM image of embedded and polished sample - Method B. T = tendon and B = bone

Method C: Cryomatrix resin embedding and cryostat sectioning

This method allowed to obtain very nice cuts of the tendon. However, as it was performed at very low temperatures, the bone was very hard and it was broken in pieces during sectioning. This was especially the problem with the thicker slices where the bone was completely ripped apart. The bone can be seen in figure 5.8a. In figure 5.8b, the broken bone can be seen, with its attachment to the tendon. Hence, on these samples the possible spatial gradient in mechanical properties could not be assessed accurately.



(a) Light microscopy image of broken bone



(b) Light microscopy image of broken bone attached to the tendon

Figure 5.8: Results of sample preparation - Method C. T = tendon and B = bone

Method D: Epoxy resin embedding and microtome sectioning

The first result that was obtained with this technique can be seen in figure 5.9. In this polarized light microscopy image, the bone can be seen on the right side and the tendon on the left side of the image. The difference in colors can be clearly seen. This result, however, is not good enough because, as can be seen, there are a lot of gaps in the tissue that make it very difficult to indent.

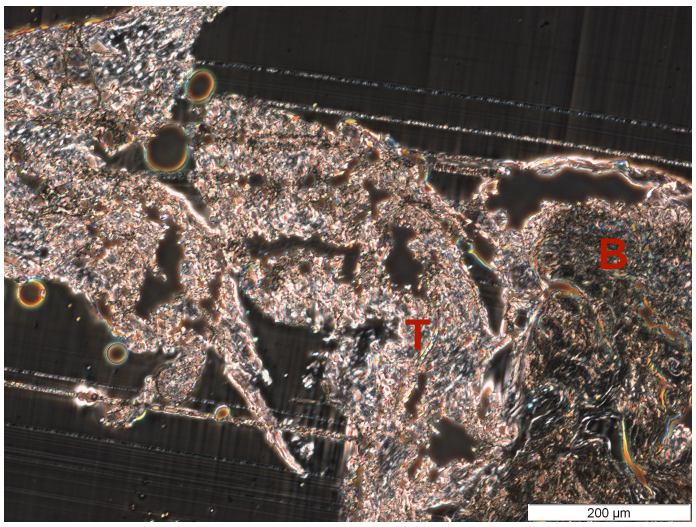
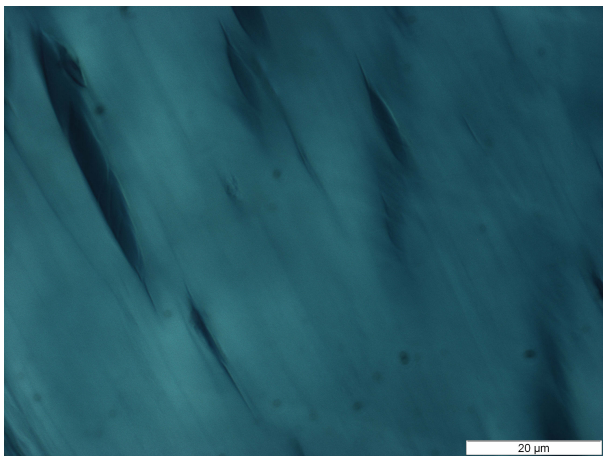
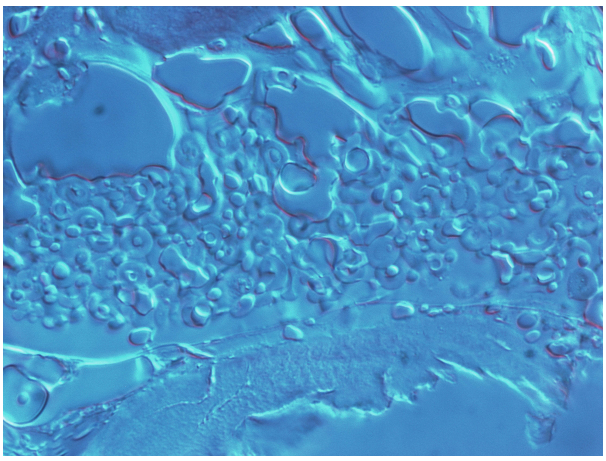


Figure 5.9: Polarized light microscopy of microtome slice of bone-tendon interface - Method D. B = bone, T = tendon

The difficulty with methods that use a saw to cut slices out of the sample is that, because of the dissimilar properties of tendon and bone, it is challenging to cut both tissues nicely. Indeed, microtome sectioning allows to obtain very nice cuts of the bone while the tendon is much harder to cut (this is also confirmed by figure 5.9). However, after optimization of this technique (method D), including, finding out how long the sample had to be dehydrated, how long the resin needed in order to fully polymerize, learning how to dissect the sample, how to position the sample for cutting, and how deep to cut, results improved. Figure 5.10 shows two differential interference contrast (DIC) microscopy images: the tendon (figure 5.10a), showing the nice alignment of the tendon collagen fibers, and the bone tissue (figure 5.10b).



(a) Tendon



(b) Bone

Figure 5.10: DIC microscopy images of tendon and bone - Method D

Method D was chosen as the method for preparing the real samples. Indeed, after optimizing this method, the results that were obtained were good for the following reasons: the surface was approximately flat and did not contain air bubbles in most cases, the biological structures were clearly visible, recognizable and intact, and the results obtained with the nanoindenter were convincing. However, still some problems were observed due to the difficulty of surface detection. This is rather complicated for very compliant tissues such as tendon. There was also a second difficulty: the test samples that were used to optimize this method were not from DIO mice. So, when this same method was used for the embedding and cutting of DIO samples, the results were not as convincing. The reason for this, is that DIO samples had a lot of adipose tissue (fat), wrapped around them, which made it very hard to dehydrate them. Because dehydration was so poor, the samples were still wet which made sectioning a lot harder than expected.

Next, a last item needed to be optimized: the surface of the sample was mostly flat thanks to the microtome, but it also needed to be horizontal when placed in the nanoindenter. As these kind of biological samples had never been used with the nanoindenter, a new method had to be designed. A house-made sample holder was used to hold the sample embedded in resin (see figure 5.11).

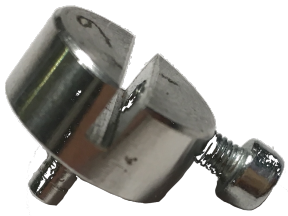


Figure 5.11: Sample holder

This sample holder with the sample were then placed in the microtome and sections were cut from the sample so that they would be perfectly horizontal, or parallel with the sample holder (the orientation of the sections can be adjusted with the microtome). Next, the sample holder was placed on a metal support, fit for the nanoindenter. This whole setup (seen in figure 5.12) was placed into the nanoindenter sample tray, ready for nanoindentation.

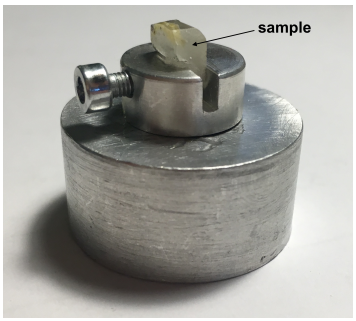


Figure 5.12: Set-up of the sample ready for indentation

5.3.2 Mechanical properties of bone-tendon interface

This section will present the results that were obtained for the nanoindentation tests using method D for sample preparation. All the images shown in this section were taken with the

microscope of the nanoindenter with 10 times magnification.

First, the modulus of the epoxy resin in which the samples were embedded was measured and was found to be equal to 3.1 GPa (figure 5.13). This was necessary in order to be able to distinguish indentation in the resin from other tissues. The light green straight line was drawn at 3.1 GPa, it can be seen that the modulus converges to this value.

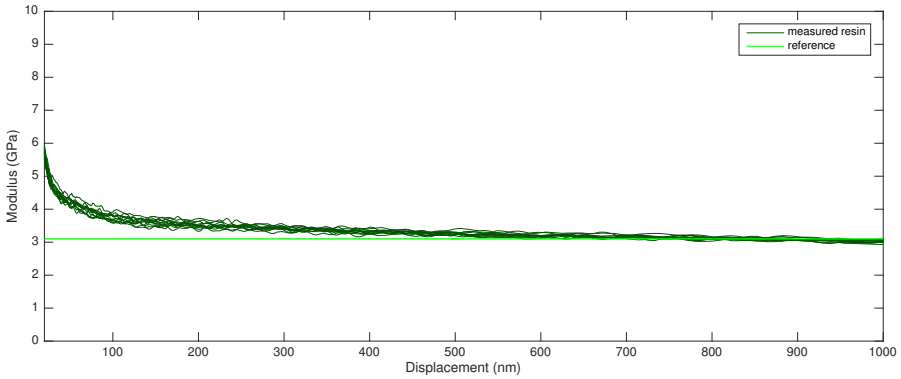


Figure 5.13: Modulus of resin in function of displacement

Figure 5.14 shows a typical load displacement curve for bone and for tendon with a displacement limit set to 1 μm during loading.

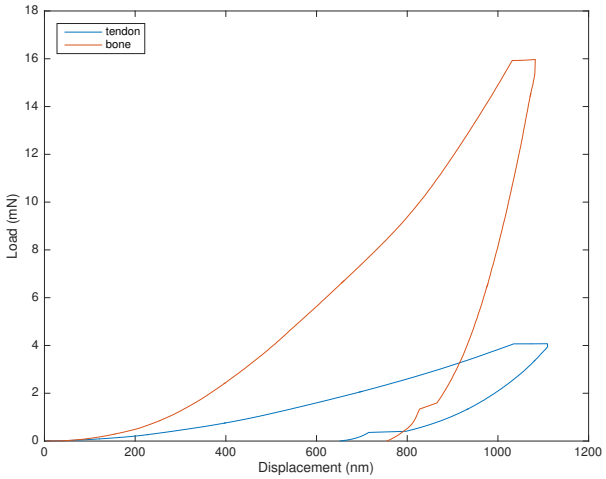


Figure 5.14: Typical load displacement curve for bone and for tendon

The next part will detail the results obtained for the bone, tendon, and at the bone-tendon interface, separately. As most tests were performed in displacement control, these results will be presented first.

Bone

Figure 5.15 displays a graph of the modulus in function of the indentation depth obtained when indenting the bone of a young sample. Each curve represents a different indent in the bone. The green line shows the modulus of the resin. Figure 5.16 is a microscopy image of the part of the bone that was indented for this sample and that allowed to obtain this graph. The dots represent

the indents that were performed and their color represents the value of the mean modulus that was observed at depths between 700 and 1000 nm (this is the region where the modulus tends to stabilize). The color scale is expressed in GPa. The black dots represent indents that were not detected. Indeed, it is important to know that when performing any nanoindentation test, there is always around 10% of the indents that are not measured or detected correctly. In this case, out of 12 indents, 3 were not detected. The modulus for the other indents is equal to 12.6 ± 1 GPa for this sample.

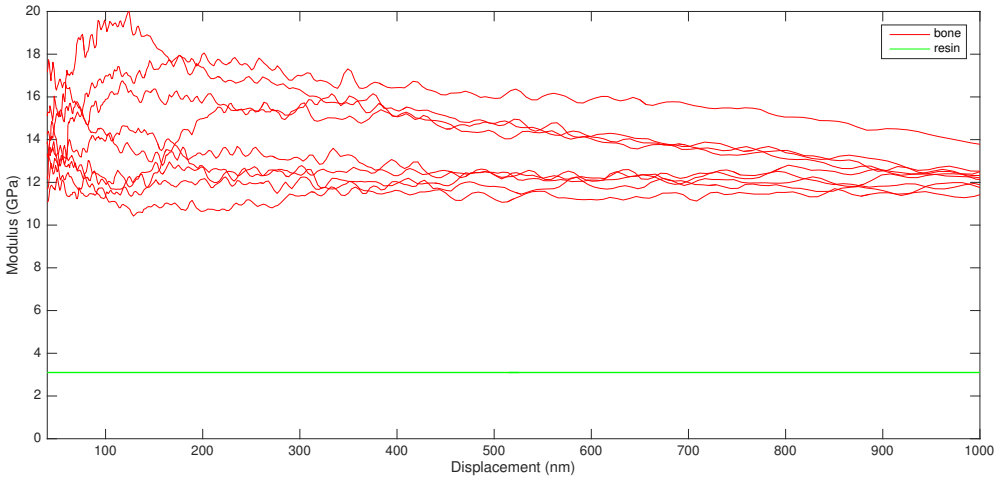


Figure 5.15: Modulus as a function of depth in the bone for a series of indents in a young sample. The green line is the modulus of resin. Method: Displacement control

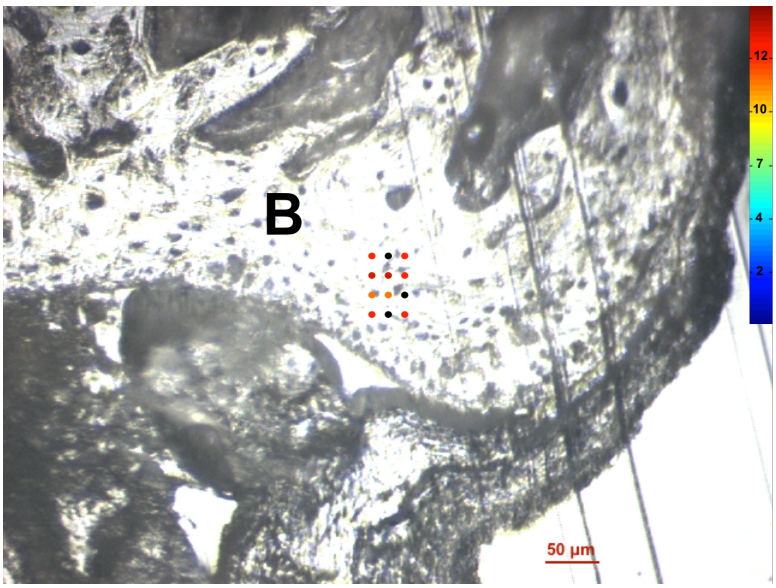


Figure 5.16: Value of the mean modulus between 700 and 1000 nm for indents in the bone of a young sample. Color scale unit is GPa. Black = indent not detected. B = bone

Tendon

The same analysis was performed on the tendon. However, for this tissue, measures were much more variable. Nevertheless, the mean modulus for all tests was always either below 0.5 GPa or between 2.5 and 4 GPa. When a modulus below 0.5 was detected this was associated to bad

surface detection. Indeed, during the analysis of the harmonic contact stiffness in function of the displacement into the surface, it could be seen that the surface was not detected correctly for those indents where a modulus below 0.5 GPa was found. However, according to literature [30], a modulus of 2.5 to 4 GPa is quite large for tendon. This could be explained by two reasons: either it means that instead of tendon, resin was detected (which has a modulus of 3.1 GPa) or it could be caused by the dehydration of the sample prior to embedding which is known to stiffen soft tissues [31] and could explain the increase in elastic modulus. As a mean value between 2.5 and 4 GPa was systematically observed even on samples were no resin was visible with the microscope, it was assumed that the modulus of tendon was increased due to the dehydration of the samples.

Figure 5.17 displays the graph of the modulus versus the displacement for the tendon of a young mouse sample. The value of the modulus is 3.5 ± 0.6 GPa between 700 and 1000 nm. Figure 5.18 shows where those indents were performed. Two indents could not be measured leaving 6 valid indents (6 curves can also be seen on the graph).

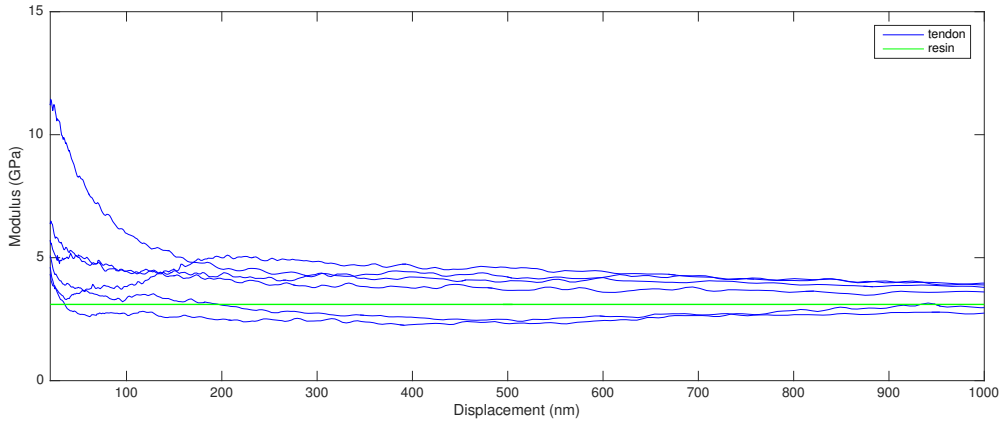


Figure 5.17: Modulus as a function of depth in the tendon for a young sample. Green line is resin. Method: Displacement control

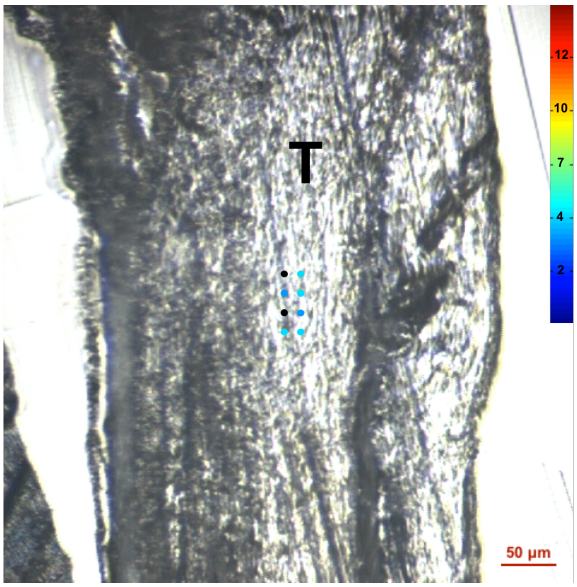


Figure 5.18: Value of the mean modulus between 700 and 1000 nm for indents in the tendon of a young sample. Color scale unit is GPa. Black = indent not detected. T = tendon

Interface

Finally, the interface was studied. An example is given for a young sample. Ten indents were performed along the interface going from bone to tendon out of which 2 indents were not detected. First, figure 5.19 depicts the load displacement curves. Three regions were defined: bone, interface, and tendon.

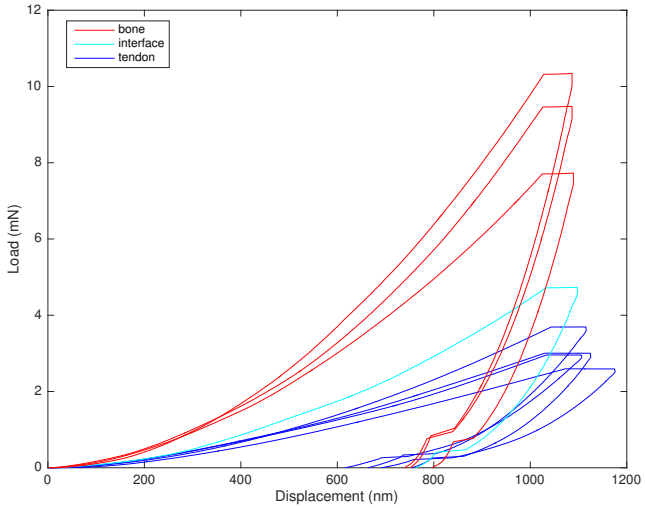


Figure 5.19: Load displacement curves for indents performed at the interface. Method: Displacement control

In figures 5.20 and 5.21, the modulus was studied for these indents. The graph of the modulus versus displacement also displays the 3 separate regions which correspond to indents shown in figure 5.21. One indent at the interface and one in the bone were not detected. The modulus is 12.9 ± 1.1 GPa for bone, 2.7 ± 0.4 GPa in tendon, and 4.7 GPa at the interface, for this sample, always computed between 700 and 1000 nm.

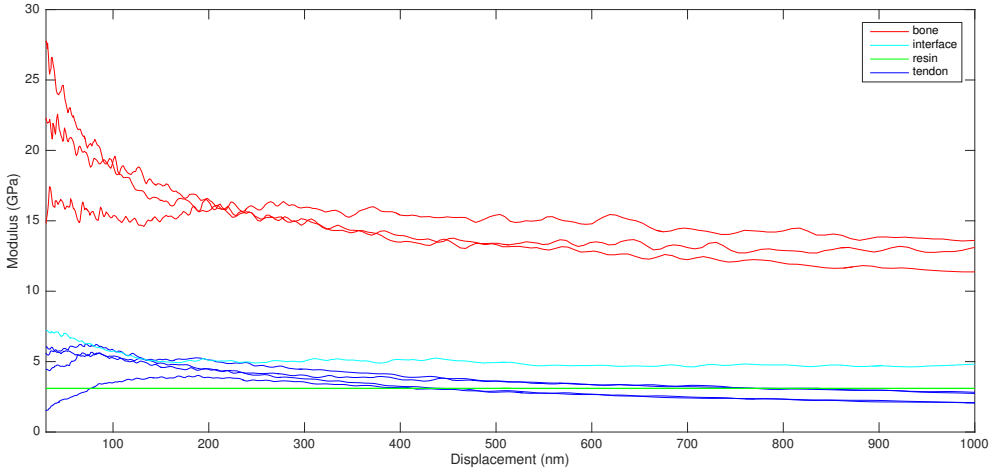


Figure 5.20: Modulus as a function of depth at the interface for a young sample. Blue lines are tendon, red lines bone, and light blue is interface. Method: Displacement control

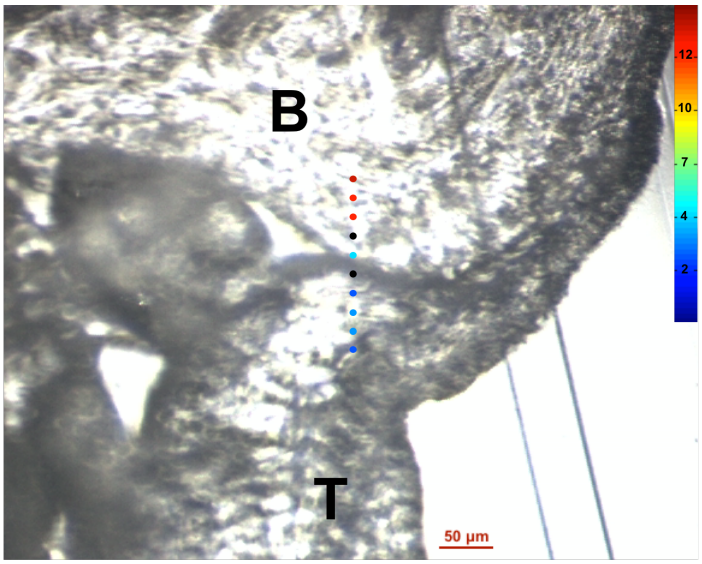


Figure 5.21: Value of the mean modulus between 700 and 1000 nm for indents at the interface, in a young sample. Color scale unit is GPa. Black = indent not detected. T = tendon and B = bone

Indentation parameters optimization

The results that were presented until now were performed with the parameters "Displacement control" from table 5.3. This worked quite well for young samples, however, for the AM and DIO samples, surface detection was not good enough, leading to too many errors. That is why surface detection needed to be improved by changing indenting parameters. It is possible to set a more sensitive criteria for surface detection, but this could lead to the indenter detecting the surface too quickly (before it actually touched the surface), just because of an impurity present in the air, for example. To prevent this, the surface approach velocity needed to be increased and with this, the initial distance between the tip and the surface was also increased. This lead to using the parameters "Displacement control with increased DSC". This way surface detection was improved for AM and DIO samples and results for young samples remained similar.

The modulus of bone was measured in an AM sample and results are displayed in figures 5.22 and 5.23. The modulus is more variable (13.2 ± 2.5 GPa) but all the indents were detected.

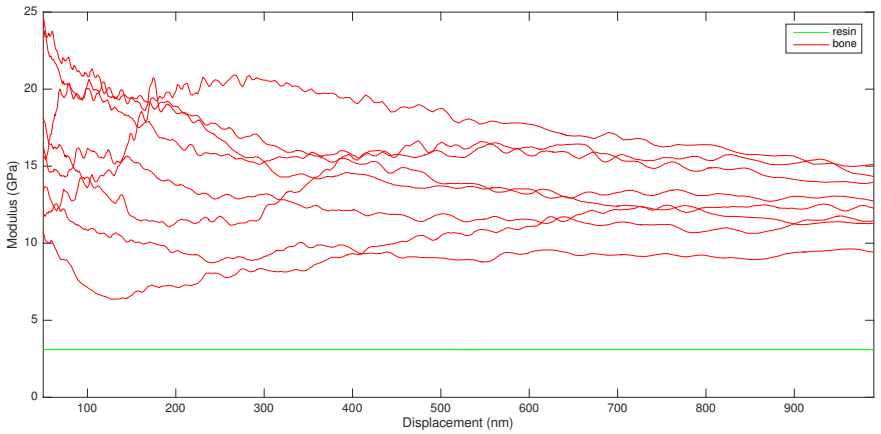


Figure 5.22: Modulus as a function of depth in the bone for an AM sample. Green line is resin. Method: Displacement control with increased DSC

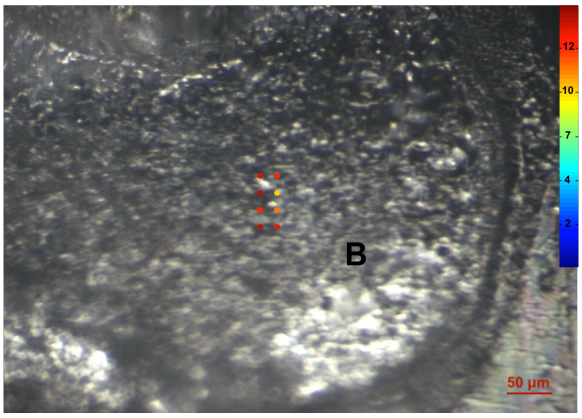


Figure 5.23: Value of the mean modulus between 700 and 1000 nm for indents in the bone of an AM sample. Color scale unit is GPa. B = bone

Figures 5.24 and 5.25 depict the results for a DIO sample. The modulus is equal to 14.7 ± 1.7 GPa and two indents were not detected.

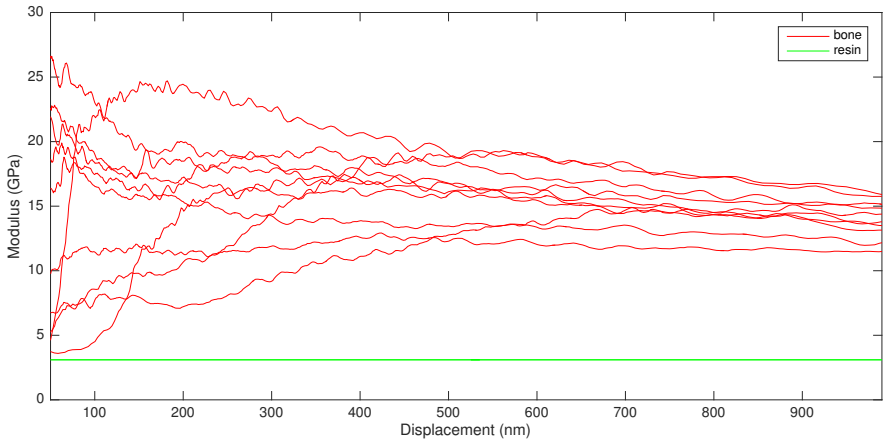


Figure 5.24: Modulus as a function of depth in the bone for a DIO sample. Green line is resin. Method: Displacement control with increased DSC

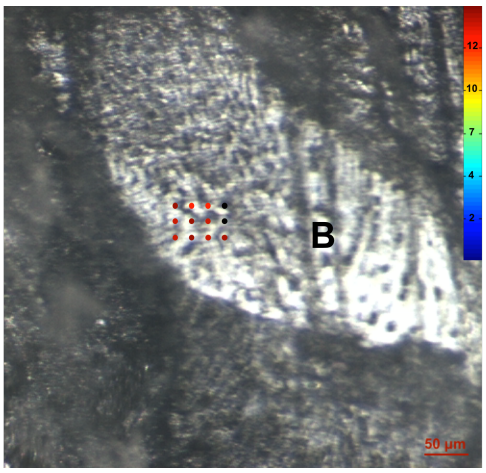


Figure 5.25: Value of the mean modulus between 700 and 1000 nm for indents in the bone, in a DIO sample. Color scale unit is GPa. Black = indent not detected. B = bone

Finally, figure 5.26 shows what was obtained indenting the tendon of an AM sample. Again, values are close to what was obtained for young samples with a modulus of 3.6 ± 0.4 GPa and correct detection of all indents.

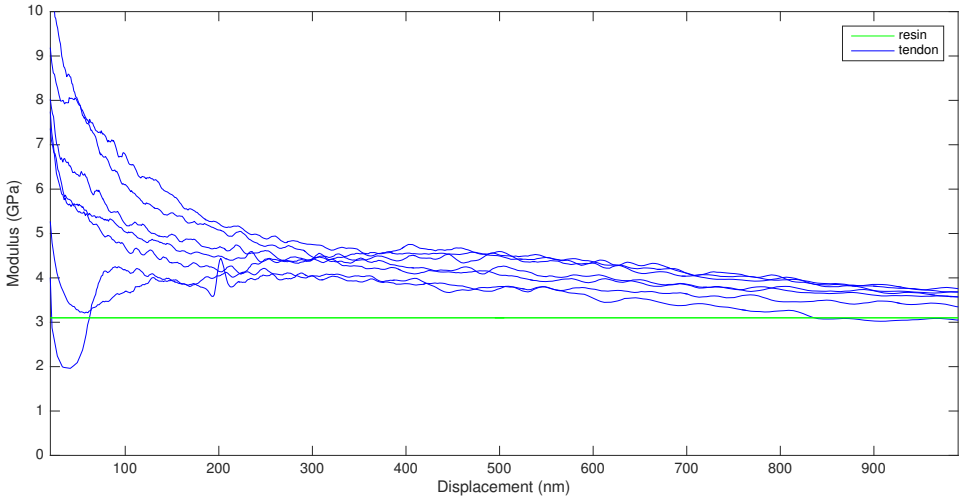


Figure 5.26: Modulus as a function of depth in the tendon for an AM sample. Green line is resin. Method: Displacement control with increased DSC

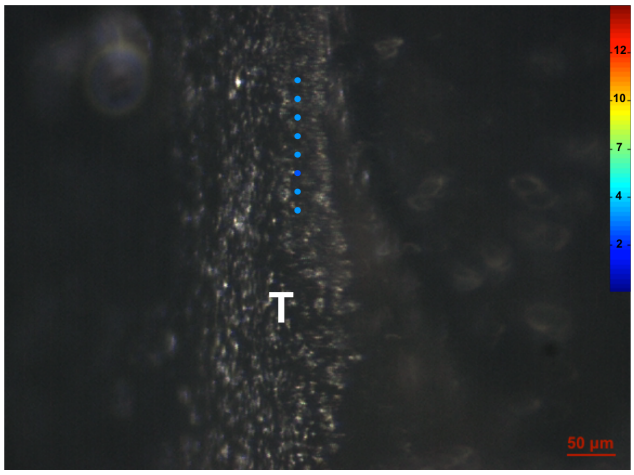


Figure 5.27: Value of the mean modulus between 700 and 1000 nm for indents in the tendon, in an AM sample. Color scale unit is GPa. T = tendon

For the DIO samples, no successful results were obtained indenting the tendon because of the amount of fat that was embedding the tendon (see figure 5.28). This means that no measurements could be performed at the interface of the DIO samples. However interface measurements were done for the AM samples.

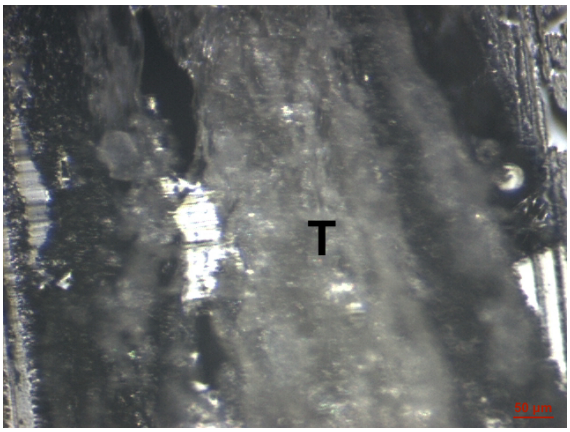


Figure 5.28: Image of the tendon in a DIO sample taken with the nanoindenter microscope. T = tendon

15 indents were placed along the interface going from bone to tendon in an AM sample (1 being bone and 15 being tendon). For clarity of the graph, only depths between 700 and 1000 nm are shown (figure 5.29). Indents 1 and 3 were not detected. The indents corresponding to this graph are shown in figure 5.30. The modulus in each region is again quite variable. For bone, it is equal to 12.8 ± 1.6 GPa (indents 1 to 7), at the interface 7.3 ± 2.1 GPa (indents 8 to 12), and in the tendon 3.1 ± 0.8 GPa (indents 13 to 15).

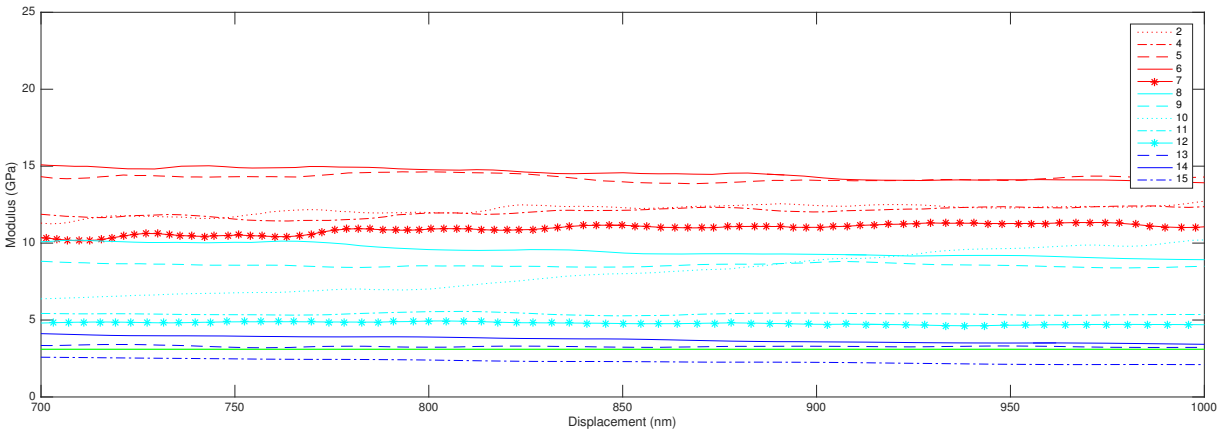


Figure 5.29: Modulus as a function of depth at the interface for an AM sample. Green line is resin. Method: Displacement control with increased DSC

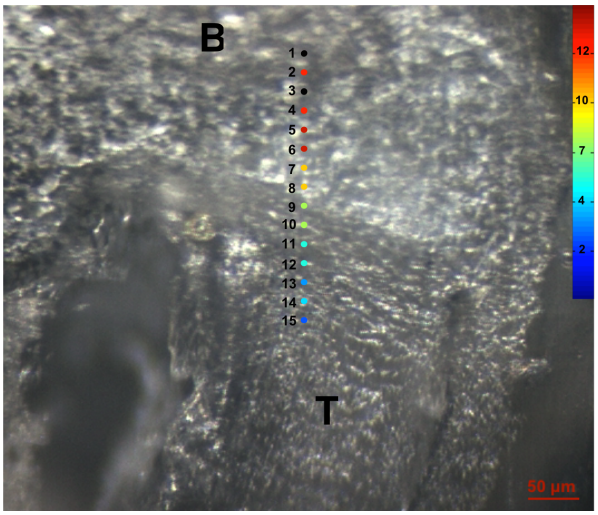
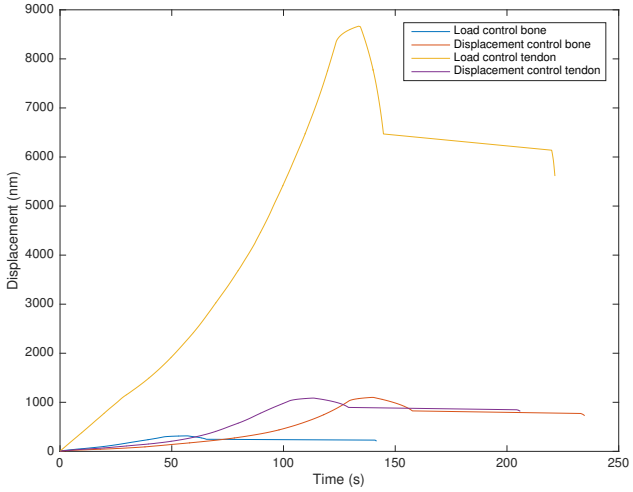
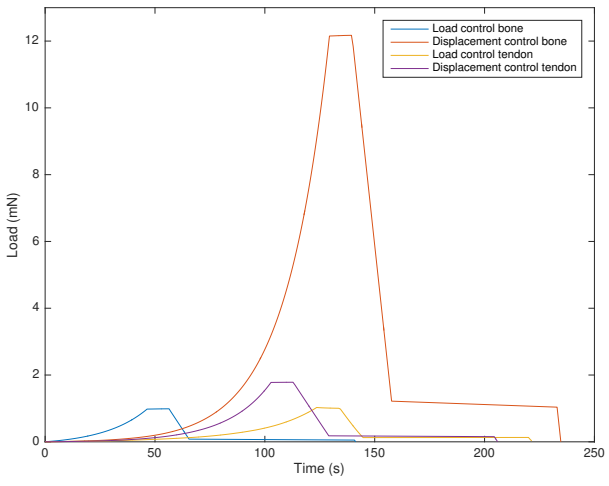


Figure 5.30: Value of the mean modulus between 700 and 1000 nm for indents at the interface, in an AM sample. Color scale unit is GPa. T = tendon, B = bone

Finally, a "Load control" method was tested on a few samples with a stopping criteria expressed in terms of load and equal to 1 mN. For comparison between load controlled and displacement controlled tests, figure 5.31 serves to study the maximum displacement and load for typical tests performed in tendon and bone. The graph of figure 5.31a displays the time versus displacement for 4 typical tests: a load controlled test for bone and for tendon and a displacement controlled test for bone and for tendon. Evidently, for the two displacement controlled tests, maximum displacement is equal to 1000 nm while the maximum displacement in load controlled test is more than 8000 nm for tendon and only around 250 nm for bone. Figure 5.31b displays the time versus load for the same four tests. The maximum load for a displacement controlled test in bone is about 12 mN while in tendon it is a bit less than 2 mN.



(a) Displacement in function of time



(b) Load in function of time

Figure 5.31: The curves represent 4 different typical tests: load control and displacement control for bone and load control and displacement control for tendon.

Figure 5.32 shows the modulus versus displacement of a test controlled in load for the bone of a DIO sample. Of course, the mean modulus cannot be taken between 700 and 1000 nm anymore. Instead, it is computed between 100 and 200 nm. Results obtained with this method were more

variable, including some outliers. The modulus is equal to 11.6 ± 5.6 GPa. Nevertheless, as can be seen in figure 5.33, all indents were detected for the bone in the DIO sample, contrary to what was obtained for the previous methods. This method should be further explored in order to obtain results with less variability.

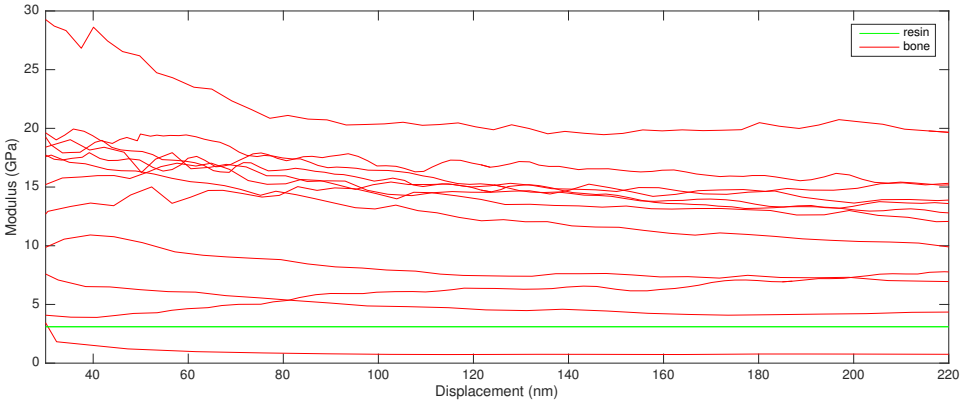


Figure 5.32: Modulus as a function of depth in the bone for a DIO sample. Green line is resin. Method: Load control

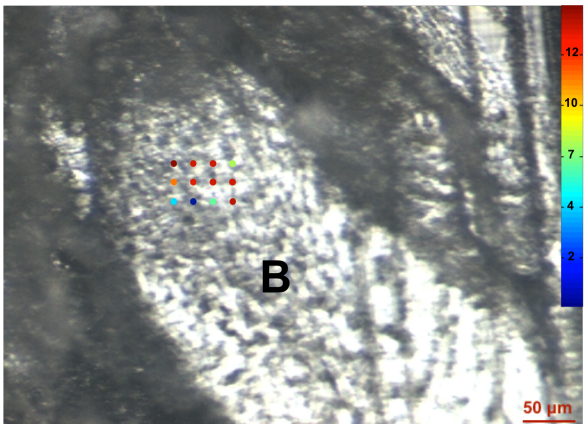


Figure 5.33: Value of the mean modulus between 100 and 200 nm for indents in the bone, in a DIO sample. Color scale unit is GPa. B = bone

Because of the rather low amount of data, it is difficult to do a statistical analysis on the results. For example, no significant differences were found in elastic modulus values of bone and tendon for the different groups. The modulus for the bone was found to be equal to 14.1 ± 2.1GPa for all methods and all samples. However, even though, not significant, it seems that the elastic modulus for the young samples is slightly lower than that of the two other groups (Young: 13.2 ± 0.8 GPa, AM: 14.4 ± 2.9 GPa, DIO: 14.7 ± 0.2 GPa), owing to the fact that in younger mice, bone is not yet fully mineralized, leading to a lower stiffness and thus a lower modulus. This confirms what has been found in earlier studies [32], where they found an increase in the bone modulus of bovine hip bones up until a certain age, after which it starts decreasing again. Note that it is important to remember that these values are not absolute values of the elastic modulus of the bone, but rather should be compared relatively to each other. The modulus is probably affected by the chemical fixation and dehydration of the samples.

5.4 Conclusion

Although differences between groups were still hard to distinguish with the results that were obtained here, values for the elastic modulus of the different tissues could be studied after optimization of both sample preparation and indentation parameters. Differences between tendon and bone could be studied and some limited tests could be performed at the interface.

The first important result that was obtained is related to sample preparation before nanoindentation. It was found that sample preparation was not necessarily the same for all groups because of the difference in morphology of the DIO samples compared to the other groups. These samples were much bigger and would have needed to be dehydrated for a much longer time before they were embedded in order to obtain nice sections with the microtome.

A second important result involves the testing parameters for nanoindentation. Indeed, the parameters that were tested on the young samples seemed to give acceptable results while this was different for the two other groups. For the DIO group, the difficulty for nanoindentation is of course mainly related to the sample preparation which was not as good as in the other groups. Despite all this, it was still possible to measure the elastic modulus in different regions of the interface and observe different values.

The modulus of the bone was easiest to evaluate as it is a stiffer material, and it is easier to obtain a flat surface from this tissue. No significant differences could be observed in bone modulus between groups, even though, it seemed that the values were a bit lower for the young samples. This, however, needs to be studied more in details in order to confirm these results. The properties of the tendon were more challenging to measure due to the very compliant nature of the tendon and the difficulty to obtain an appropriate surface for indentation. Some measures were possible in the young and AM samples but not enough to be able to compare values between groups.

Tests were also performed along the interface to look at the changes through the different regions. The four regions bone, MF, NMF, and tendon were classified into three regions as bone, interface, and tendon. This allowed to observe a change in the modulus going from bone to tendon in the young and AM samples. The modulus of bone was the highest, followed by that of the interface, and the modulus of the tendon was the lowest. This shows that the stiffness of the interface is intermediate to that of the tendon and the bone, allowing to minimize stress concentrations at the insertion site to allow these two tissues to function together in unison.

Chapter 6

Conclusion

Chapters 4 and 5 described the experiments and results obtained for micro-computed tomography and nanoindentation, respectively. The aim of this chapter is to bring these previous chapters together in one general discussion followed by some future perspectives for both techniques and a final conclusion.

6.1 General discussion

Before micro-computed tomography and nanoindentation could be applied to the samples, there was need for optimization of both techniques. First, regarding micro-computed tomography, it was necessary to learn how to dissect the samples to obtain a better resolution by isolating only the tissue of interest and it was important to learn how to interpret the data once acquired. Regarding sample preparation for nanoindentation, it was soon clear that this is non trivial for heterogeneous biological samples, such as the bone-tendon interface which is made of tissues with very different mechanical properties. Adding to this difficulty is the fact that the area of interest is only a few hundreds of microns in size. It proved important to find a method that would allow to obtain a surface that could be indented. Sectioning the embedded samples worked better than polishing in order to avoid artifacts or impurities to enter the samples. Despite the challenges that were encountered when performing nanoindentation on biological tissues, it was possible to acquire information on the differences in mechanical properties of the different regions. After optimization of data interpretation for micro-computed tomography and optimization of sample preparation and testing methodology for nanoindentation, both techniques were validated as appropriate for high-resolution analysis of the 3D properties of biological tissues. Indeed, these techniques allowed to acquire micro and nano-scale information on the structure, composition, dimensions and mechanical properties of the bone-tendon interface.

In addition to optimizing these techniques, the goal was to find differences in interface properties related to age and obesity. Chapter 4 was devoted to the analysis of the structural properties and from the data acquired it was possible to come to the following conclusions. The bone-tendon interface is composed of four regions. No gradation in mineral content was found in those regions. Instead a sharp transition between mineralized (bone and MF) and non mineralized (NMF and tendon) regions was found for all groups. No significant changes were observed at the interface between young and aged groups. However, some differences were observed between the aged group and the aged group with obesity-driven type 2 diabetes. Indeed, the region of the interface, called the mineralized fibrocartilage, was found to be wider for the DIO group due to a delay in chondrogenesis and the increased load applied to their skeleton. The tendon was found to be thicker due to the non-enzymatic glycation of collagen fibers and also due to the increased load applied on the body of the diabetic models. Collagen fibers were found to be perpendicular to the interface for the young and AM groups. In the DIO group the fibers

were perpendicular to the interface in the MF but it was not possible to observe their orientation in the NMF. Chapter 5 was dedicated to the mechanical properties through nanoindentation and made it possible to obtain high-resolution measurements of the modulus of the different tissues involved in the bone-tendon interface. The modulus of bone was the largest, that of the interface was intermediate, and the modulus of the tendon was the lowest. For both techniques, it was concluded that the DIO samples were the most difficult to analyze. It was challenging to find the fiber orientation of these samples on the μCT scans and it was difficult to obtain the mechanical properties of the samples through nanoindentation because of the difficulty to section them. This is caused by their distinct morphology compared to the two other groups.

Future studies and more in depth analysis of the interface following the methods that were studied and applied here will likely lead to new insight into development of improved surgical solutions for the replacement of the bone-tendon interface. To that end, some future perspectives are given in the next section.

6.2 Future perspectives

The results that were obtained in this thesis using μCT, CE-CT and nanoindentation provide interesting perspectives for the future and also seem to correlate well with what already has been found earlier. However, in future experiments, it would be useful to use a larger amount of samples to obtain a better statistical significance. It would also be of interest to study different anatomical locations and compare them with the Achilles tendon-to-bone insertion. This could also be done in different species, including in human tissue. To do a more detailed study on the influence of age, more age groups should be investigated. Other pathologies or diseases could also be studied. In the next part of this section, more specific future perspectives are given for μCT and CE-CT and for nanoindentation, separately.

6.2.1 μCT and CE-CT

First, to look more into details at the mineralization degree and how it is affected by ageing or pathologies, Raman spectroscopy could be used in the future in parallel with μCT. It allows to perform a sensitive analysis of the composition and structure of materials in a non-destructive way.

Second, to more rigorously evaluate the dimensions of the mineralized fibrocartilage of the interface, automated or semi-automated segmentation could be used to distinguish this region from the bone in the μCT scans instead of doing this manually.

Third, the contrast agent that was used for staining the samples for CE-CT, Lugol's iodine solution, is a nice contrast agent for visualization of the structures in the tendon, however, one of its major drawbacks is that it dehydrates the samples when used. This is something that should be taken into account in the future, and maybe a contrast agent could be found that does not have this effect.

Lastly, more advanced analysis should be done on the CE-CT scans to study the collagen fiber orientation and to be able to distinguish the non mineralized fibrocartilage from the tendon. This could also be done using different techniques, such as, microscopy or second harmonic generation imaging (microscope imaging technique that obtains contrasts from variations in a specimen's ability to generate second-harmonic light from the incident light).

6.2.2 Nanoindentation

Sample preparation for nanoindentation was tested on test samples before embedding the real samples. As none of the test samples were DIO samples, it was not anticipated that the preparation could be different for DIO samples. It was, however, the case because of the large amount of fat that was present in these samples. For the preparation of these types of samples, another method should be used. A possible solution could be to dehydrate these samples with acetone, in order to remove all the fat, and then embed them in another type of resin, such as paraffin or a polyester vestopal type of resin.

Another challenge was to make sure indentation was done in tissue and not in the resin in which the samples were embedded. To prevent from indenting the resin, a solution, in the future, could be to color the resin to make it easier to distinguish the biological tissue from the resin.

Nanoindentation was performed on fixed and dehydrated samples which could affect the mechanical properties of the tissues. It would be interesting to repeat these experiments on fresh samples for comparison. This means that tests would need to be performed right after harvesting of the tissue and that no dehydration step could be performed, so another sample preparation method should be used.

A Poisson ratio of 0.5 was selected for the interface. However, in [8], they found through numerical simulations that stress concentrations at the interface are reduced by varying Poisson's ratio along the insertion site which is most probably the case of the natural interface and could be taken into account in the future when computing the elastic modulus of the interface. To do this, however, Poisson's ratio of the interface would need to be computed experimentally.

Next, another challenge was to detect the surface of the sample correctly. A Berkovich tip was used for all the experiments. A possible solution to improve surface detection could be to use a flat punch tip, which has a larger contact area at the moment it starts to enter the material. However, it is not certain that this kind of tip would work well in very soft tissue such as tendon. Additionally, using this tip would greatly decrease the resolution compared to a Berkovich tip.

A last future perspective that could improve nanoindentation on these types of samples could be to use a different type of indenter: one that performs nanoindention on samples immersed in liquid. Indeed, difficulties due to surface tension can be overcome when tip and sample are both immersed for testing.

6.3 Final conclusion

The goal of this thesis was to characterize the bone-tendon interface, a site that is prone to injury due to its complicated structure capable of mediating load between tendon and bone, two very dissimilar tissues. In order to meet this goal, several testing methods were first optimized and then applied on different mice groups. They include micro-computed tomography and contrast-enhanced computed tomography for analysis of the composition and structure of the tissue and nanoindentation for mechanical characterization.

Promising results were obtained with both techniques. Micro-computed tomography allowed highly detailed visualization of the structures at the interface and by doing data analysis, it was possible to characterize the interface physical dimensions, porosity and the dimensions of the tendon. It was also possible to visualize the fiber orientation both in the tendon and at the interface. Sample preparation was optimized for nanoindentation, and by testing several indentation parameters, values for the elastic modulus of the different tissues present at the interface were found.

In conclusion, the properties of the bone-tendon interface were investigated by suggesting and optimizing recent techniques for three-dimensional high-resolution characterization. Further research should focus on the use of fresh samples and repeating tests with a larger amount of samples.

Bibliography

[1] Lester Smith, Younan Xia, Leesa M. Galatz, Guy M. Genin, and Stavros Thomopoulos. Tissue-engineering strategies for the tendon/ligament-to-bone insertion. *Connective Tissue Research*, 53(2):95–105, 2011.

[2] Guy M. Genin, Alistair Kent, Victor Birman, Brigitte Wopenka, Jill D. Pasteris, Pablo J. Marquez, and Stavros Thomopoulos. Functional grading of mineral and collagen in the attachment of tendon to bone. *Biophysical Journal*, 97(4):976–985, 2009.

[3] Donna M. Ebenstein and Lisa A. Pruitt. Nanoindentation of biological materials. *Nano Today*, 1(3):26–33, 2006.

[4] Paxton Jennifer Z. MSC, PhD. The unique anatomy of tissue interfaces, paxton laboratory.

[5] Yanxin Liu, Victor Birman, Changqing Chen, Stavros Thomopoulos, and Guy M. Genin. Mechanisms of bimaterial attachment at the interface of tendon to bone. *Journal of Engineering Materials and Technology*, 133(1):011006, 2011.

[6] John Apostolakos. The enthesis: a review of the tendon-to-bone insertion. *Muscles, Ligaments and Tendons Journal*, 2014.

[7] K. L. Moffat. Characterization of the structure-function relationship at the ligament-to-bone interface. *Proceedings of the National Academy of Sciences*, 105(23):7947–7952, 2008.

[8] Y.x. Liu, S. Thomopoulos, V. Birman, J.-S. Li, and G.m. Genin. Bi-material attachment through a compliant interfacial system at the tendon-to-bone insertion site. *Mechanics of Materials*, 44:83–92, 2012.

[9] I-Ning E. Wang, Siddarth Mitroo, Faye H. Chen, Helen H. Lu, and Stephen B. Doty. Age-dependent changes in matrix composition and organization at the ligament-to-bone insertion. *Journal of Orthopaedic Research*, 24(8):1745–1755, 2006.

[10] G. Kerckhofs, M. Durand, R. Vangoitsenhoven, C. Marin, B. Van Der Schueren, G. Carmeliet, F. P. Luyten, L. Geris, and K. Vandamme. Changes in bone macro- and microstructure in diabetic obese mice revealed by high resolution microfocus x-ray computed tomography. *Scientific Reports*, 6(1), 2016.

[11] Gladys L.y. Cheing, Rosanna M.w. Chau, Rachel L.c. Kwan, Cheung-Hei Choi, and Yong-Ping Zheng. Do the biomechanical properties of the ankle–foot complex influence postural control for people with type 2 diabetes? *Clinical Biomechanics*, 28(1):88–92, 2013.

[12] Brianne K. Connizzo, Pankti R. Bhatt, Kenneth W. Liechty, and Louis J. Soslowsky. Diabetes alters mechanical properties and collagen fiber re-alignment in multiple mouse tendons. *Annals of Biomedical Engineering*, 42(9):1880–1888, 2014.

[13] J.m. Pritchard, A. Papaioannou, C. Tomowich, L.m. Giangregorio, S.a. Atkinson, K.a. Beattie, J.d. Adachi, J. Debeer, M. Winemaker, V. Avram, and et al. Bone mineralization is

elevated and less heterogeneous in adults with type 2 diabetes and osteoarthritis compared to controls with osteoarthritis alone. *Bone*, 54(1):76–82, 2013.

[14] Jeffrey P. Spalazzi, Adele L. Boskey, Nancy Pleshko, and Helen H. Lu. Quantitative mapping of matrix content and distribution across the ligament-to-bone insertion. *PLoS ONE*, 8(9), Mar 2013.

[15] Jonathan M. Hurng, Michael P. Kurylo, Grayson W. Marshall, Samuel M. Webb, Mark I. Ryder, and Sunita P. Ho. Discontinuities in the human bone–pdl–cementum complex. *Biomaterials*, 32(29):7106–7117, 2011.

[16] Yanxin Liu, Andrea G. Schwartz, Victor Birman, Stavros Thomopoulos, and Guy M. Genin. Stress amplification during development of the tendon-to-bone attachment. *Biomechanics and Modeling in Mechanobiology*, 13(5):973–983, 2013.

[17] Paul M. Gignac and Nathan J. Kley. Iodine-enhanced micro-ct imaging: Methodological refinements for the study of the soft-tissue anatomy of post-embryonic vertebrates. *Journal of Experimental Zoology Part B: Molecular and Developmental Evolution*, 322(3):166–176, 2014.

[18] Greet Kerckhofs, Steve Stegen, Nick van Gastel, Annelies Sap, Guillaume Falgayrac, Guillaume Penel, Marjorie Durand, Frank P. Luyten, Liesbet Geris, Katleen Vandamme, Tatjana Parac-Vogt, and Geert Carmeliet. Simultaneous three-dimensional visualization of mineralized and soft skeletal tissues by a novel microct contrast agent with polyoxometalate structure.

[19] Oliver E. Armitage and Michelle L. Oyen. Indentation across interfaces between stiff and compliant tissues. *Acta Biomaterialia*, 56:36–43, 2017.

[20] K.n. Hauch, M.l. Oyen, G.m. Odegard, and T.l. Haut Donahue. Nanoindentation of the insertional zones of human meniscal attachments into underlying bone. *Journal of the Mechanical Behavior of Biomedical Materials*, 2(4):339–347, 2009.

[21] Ewa M. Spiesz, Paul Roschger, and Philippe K. Zysset. Elastic anisotropy of uniaxial mineralized collagen fibers measured using two-directional indentation. effects of hydration state and indentation depth. *Journal of the Mechanical Behavior of Biomedical Materials*, 12:20–28, 2012.

[22] Sunita P Ho, Michael P Kurylo, Kathryn Grandfield, Jonathan Hurng, Ralf-Peter Herber, Mark I Ryder, Virginia Altoe, Shaul Aloni, Jian Q Feng, Samuel Webb, et al. The plastic nature of the human bone-periodontal ligament-tooth fibrous joint. *Bone*, 57(2):455–467, 2013.

[23] Greet Kerckhofs. *Morphological and Mechanical Quantification of Porous Structures by means of Micro-CT*. PhD thesis, Katholieke Universiteit Leuven, 2009.

[24] Shailesh Agarwal, Shawn Loder, John Li, Cameron Brownley, Jonathan R. Peterson, Eboda Oluwatobi, James Drake, David Cholok, Kavitha Ranganathan, Hsiao Hsin Sung, and et al. Diminished chondrogenesis and enhanced osteoclastogenesis in leptin-deficient diabetic mice (ob/ob) impair pathologic, trauma-induced heterotopic ossification. *Stem Cells and Development*, 24(24):2864–2872, 2015.

[25] Astrid Liedert, Daniela Kaspar, Peter Augat, Anita Ignatius, and Lutz Claes. Mechanobiology of bone tissue and bone cells. 2005.

[26] B J Briscoe, L Fiori, and E Pelillo. Nano-indentation of polymeric surfaces. *Journal of Physics D: Applied Physics*, 31(19):2395–2405, Jul 1998.

[27] H.s. Gupta, S. Schratter, W. Tesch, P. Roschger, A. Berzlanovich, T. Schoeberl, K. Klaushofer, and P. Fratzl. Two different correlations between nanoindentation modulus and mineral content in the bone–cartilage interface. *Journal of Structural Biology*, 149(2):138–148, 2005.

[28] Yu-Shu Lai, Wen-Chuan Chen, Chang-Hung Huang, Cheng-Kung Cheng, Kam-Kong Chan, and Ting-Kuo Chang. The effect of graft strength on knee laxity and graft in-situ forces after posterior cruciate ligament reconstruction. *Plos One*, 10(5), 2015.

[29] Leann M. Dourte, Lydia Pathmanathan, Michael J. Mienaltowski, Abbas F. Jawad, David E. Birk, and Louis J. Soslowsky. Mechanical, compositional, and structural properties of the mouse patellar tendon with changes in biglycan gene expression. *Journal of Orthopaedic Research*, 31(9):1430–1437, 2013.

[30] Ryuichi Sasaki Toshiyuki Kurihara and Tadao Isaka. Mechanical properties of achilles tendon in relation to various sport activities of collegiate athletes. *30th Annual Conference of Biomechanics in Sports*, 2012.

[31] S. Nicolle and J.-F. Palierne. Dehydration effect on the mechanical behaviour of biological soft tissues: Observations on kidney tissues. *Journal of the Mechanical Behavior of Biomedical Materials*, 3(8):630–635, 2010.

[32] Waseem Ur R. Effect of age on the elastic modulus of bone. *Journal of Bioengineering and Biomedical Science*, 07(01):630–635, 2017.

Appendix A

Abstract

Nanoindentation of biological tissues: opportunities and challenges for the bone-tendon interface

Lisa Leyssens[1], Sophie Ryelandt[1], Audrey Favache[1], Greet Kerckhofs[1 2 3]

[1]Institute of Mechanics, Materials, and Civil Engineering, Université Catholique de Louvain, Louvain-la-Neuve, Belgium
[2]Dept. Materials Science and Engineering, KU Leuven, Leuven, Belgium
[3]Prometheus, Division of Skeletal Tissue Engineering, KU Leuven, Leuven, Belgium

INTRODUCTION

Both for the design and evaluation of medical devices or implants/biomaterials and for the replacement of biological tissues, it is necessary to understand the biomechanical characteristics of the tissues to be replaced. Additionally, a change in the mechanical properties of biological tissues can be an important indication of a disease or a pathology. Mechanical testing of biological tissues is, therefore, a critical step in the design and evaluation of medical devices, as well as in improving the understanding of certain diseases. Biological tissues, however, have a non-elastic behavior, and thus there is a need for proper mechanical testing methodologies, set-ups and protocols.

The goal of this study was to evaluate the rate of change in mechanical properties within the transition region between the bone and the tendon, or the bone-tendon interface, which has a function of mediating load between two very dissimilar tissues: the bone which is hard and stiff, and the tendon which is a soft tissue. Injuries occurring at this site commonly result in pain, disability and significant medical costs. The chances of failure of a surgical intervention can be very high, making the bone-tendon interface an important research topic. Characterizing its mechanical properties should, in the future, help to optimally reproduce the original tissue through tissue engineering to allow for successful repair (Smith et al. 2011).

The objective was to optimize the sample preparation for nanoindentation of the bone-tendon interface at the site of the Achilles tendon-to-heel bone in mice, which is only a few hundreds of microns long (approx. 200 μm), and to investigate the change in mechanical properties going from tendon to bone and correlate this change with the change in mineralization content and in collagen fiber orientation. Nanoindenta-

tion has recently emerged as a powerful method for mechanical characterization of biological tissues (Ebenstein and Pruitt 2006). It allows to assess the tissues at high resolution and in different directions, and it can be used to characterize complicated local mechanical properties of heterogeneous materials (Hauch et al. 2009). However, although sample preparation is a crucial step, it is non-trivial for small biological tissues with heterogeneous properties.

MATERIALS AND METHODS

Bone-tendon interfaces were extracted from mice and were fixed in 4% paraformaldehyde. The aim of sample preparation was to obtain a flat surface that showed both the tendon and the bone, placed in the correct direction so that the interface between them could be indented. Three main sample preparation techniques were evaluated: (A) resin embedding and polishing, (B) resin embedding and cryostat sectioning, and (C) resin embedding and microtome sectioning.

RESULTS AND DISCUSSION

In method A, epoxy resin embedding was done in vacuum. Polishing was performed using 1 μm grain size grinding paper. This method showed unsatisfactory results. First, the embedding was challenging due to the difficulty of positioning the sample as desired, so that it would be at the surface of the resin. Second, polishing was problematic because of impurities and bubbles that were entering the resin, and because of the high chances of damaging the sample. In method B, the samples were cooled down in ice for 15-20 minutes after embedding. Cutting could then be performed with a cryostat (*Leica CM3050 S*) at -24°C. Slices of different thicknesses were obtained ranging from 25 μm up to 200 μm. The problem with this method was that the bone became very hard compared to the tendon at these low temperatures, making it very hard to cut the tissue without ripping of the bone. Method C involved dehydrating the sample in ethanol prior to embedding in epoxy resin, followed by cutting a slice from the sample with a microtome (*Leica EM UC6*) equipped with a diamond saw. The slice was then placed on a glass slide. Nanoindentation could not be performed on the slice itself as it was too thin (less than 1 μm thick). The remaining embedded part of the sample was placed in epoxy resin again in order to fill the remaining holes and pores and some slices were again cut from the sample. The remaining surface of the sample was entirely flat, making it possible to indent. As no polishing or cooling was required, better results were obtained: the biological structures were clearly visible, recognizable and intact. With this preparation method, distinct properties could be detected with nanoindentation.

CONCLUSION

Nanoindentation on biological tissues is a newly emerging technique and therefore, protocols for sample preparation still need to be optimized, especially for micrometer-scale, heterogeneous tissues. In this study, sample preparation for nanoindentation was optimized for the mouse Achilles tendon-to-bone interface, showing a change in mechanical properties.

REFERENCES

Ebenstein, D. M. and Pruitt, L. A. (2006). "Nanoindentation of biological materials." *Nano Today*, 1(3), 2633.

Hauch, K., Oyen, M., Odegard, G., and Donahue, T. H. (2009). "Nanoindentation of the insertional zones of human meniscal attachments into underlying bone." *Journal of the Mechanical Behavior of Biomedical Materials*, 2(4), 339347.

Smith, L., Xia, Y., Galatz, L. M., Genin, G. M., and Thomopoulos, S. (2011). "Tissue-engineering strategies for the tendon/ligament-to-bone insertion." *Connective Tissue Research*, 53(2), 95105.

Rue Archimède, 1 bte L6.11.01, 1348 Louvain-la-Neuve **www.uclouvain.be/epl**

